Filtering & Identification for Spline based Wavefront Reconstruction in Adaptive Optics

Erwin de Gelder

Master of Science Thesis

TU Delft Delft University of Technology

Delft Center for Systems and Control

Filtering & Identification for Spline based Wavefront Reconstruction in Adaptive Optics

Master of Science Thesis

For the degree of Master of Science in Systems and Control at Delft University of Technology

Erwin de Gelder

October 22, 2014

Faculty of Mechanical, Maritime and Materials Engineering (3mE) · Delft University of Technology

Delft University of Technology
Department of
Delft Center for Systems and Control (dcsc)

The undersigned hereby certify that they have read and recommend to the Faculty of Mechanical, Maritime and Materials Engineering (3mE) for acceptance a thesis entitled

Filtering & Identification for Spline based Wavefront Reconstruction in Adaptive Optics

by

Erwin de Gelder

in partial fulfillment of the requirements for the degree of

Master of Science Systems and Control

Dated: October 22, 2014

Supervisor(s):

prof.dr.ir. M. Verhaegen

Reader(s):

dr.ir. V.A. Korkiakoski

dr.ir. C.C. de Visser

ir. A.E. Brunner

Abstract

Without any form of compensation, atmospheric turbulence blurs the images obtained by ground-based telescopes. An Adaptive Optics (AO) system compensates for the optical wavefront distortions introduced in a light beam as it propagates through a turbulent medium. The wavefront phase errors are measured with a Wavefront Sensor (WFS) and corrected by adding the conjugated phase with an actuator such as a Deformable Mirror (DM). This graduation project focuses on the reconstruction of the wavefront using a Shack-Hartmann (SH) WFS, while taking its spatial and temporal dynamics into account.

The recently introduced Spline based ABerration REconstruction (SABRE) is used to model the spatial dynamics using the approximated slopes. It has been shown that using the measured intensity pattern of the WFS, rather than the approximated slopes (which are obtained using a centroid algorithm), the WFR can be improved, because the intensity distribution contains more information than the approximated slopes. This, however, has been demonstrated using a Hartmann sensor. The first contribution of this thesis was to adapt the method for the SH WFS, which is the commonly used sensor in astronomy. This is achieved by using an additional image of a SH WFS under the same conditions, but with an additional known aberration. The prescribed algorithms are tested with the AO simulation tool Yao. It is shown that for small aberrations, SABRE with intensity measurements provides more accurate reconstructions of the wavefront.

Because of a delay, caused by the WFS and WFR, an error is introduced resulting from the temporal dynamics of the wavefront. The second goal of this thesis is to predict the wavefront aberrations, such that the temporal dynamics are taken into account. Furthermore, the prediction should exploit the local nature of SABRE, such that it is applicable for parallel programming. Subspace Identification (SID) is employed for estimating the model of the temporal dynamics. The estimated model is used by a Kalman Filter (KF) to predict the wavefront aberration. The SID and KF are adapted to methods which are compliant with the local nature of SABRE and therefore, the presented SID and KF are suitable for parallel programming. The SID and KF are tested and tuned with both methods of SABRE, i.e. SABRE with the approximated slopes and SABRE with the measured intensities. It is demonstrated that the KF predicts the aberration significantly more accurate compared to the delayed reconstruction and at times even outperforms the reconstruction without delay.

Table of Contents

Acknowledgements **xiii**

1 Introduction **1**
1-1 Problem statement . . . 3
1-2 Thesis layout . . . 3

2 Motivation **5**
2-1 The need for Adaptive Optics . . . 5
2-2 Principle of adaptive optics . . . 6
2-3 Control objective of adaptive optics . . . 7
2-4 Scope of the thesis . . . 8
2-4-1 Wavefront Reconstruction . . . 9
2-4-2 Subspace Identification . . . 10
2-4-3 Kalman Filtering . . . 12

3 Wavefront Reconstruction with SABRE **13**
3-1 Introduction . . . 13
3-2 Wavefront Reconstruction principles . . . 14
3-2-1 Optical Image Formation . . . 14
3-2-2 Different methods for Wavefront Reconstruction . . . 15
3-3 Spline Based Aberration Reconstruction . . . 17
3-3-1 Bivariate simplex B-splines . . . 17
3-3-2 SABRE with gradient measurements . . . 18
3-3-3 SABRE with intensity measurements . . . 19
3-4 Experiments with Yao . . . 21
3-4-1 Description of experiments . . . 22
3-4-2 Example of one experiment . . . 25

3-4-3 Effect of defocus on intensity based SABRE . . . 26
3-4-4 Triangulation . . . 27
3-4-5 Effect of Fried parameter r_0 and the amount of sub-apertures . . . 28
3-4-6 Effect of noise . . . 29
3-5 Conclusion . . . 31

4 Autonomous Subspace Identification **33**
4-1 Introduction . . . 33
4-2 System description, assumptions and notations . . . 33
4-3 Autonomous Subspace Identification . . . 34
4-3-1 Past Output Autonomous Subspace Identification . . . 34
4-3-2 Autonomous Predictor Based Subspace Identification . . . 37
4-4 Preliminary Simulation . . . 39
4-4-1 Description . . . 39
4-4-2 Results ASID . . . 39

5 Filtering of SABRE **43**
5-1 Problem description . . . 43
5-2 Constrained Kalman Filtering for SABRE . . . 44
5-2-1 Centralized CKF . . . 44
5-2-2 Distributed CKF . . . 45
5-2-3 State projection . . . 46
5-2-4 State projection with Piston Mode Equalization . . . 47
5-2-5 State projection using ADMM . . . 48
5-3 Experiments with Yao . . . 51
5-3-1 Description of experiments . . . 51
5-3-2 Choosing the sample time . . . 53
5-3-3 Choosing the system order n . . . 53
5-3-4 Influence of past and future windows p and f . . . 54
5-3-5 Influence of weighting matrix W . . . 56
5-3-6 Constrained Kalman Filtering versus Kalman Filtering . . . 57
5-3-7 State projection with Piston Mode Equalization . . . 58
5-4 Conclusion . . . 58

6 Conclusions and Recommendations **61**
6-1 Conclusions . . . 61
6-2 Recommendations & Future work . . . 63

A Simulations with Yao **65**
A-1 What is Yao? . . . 65
A-2 Why Yao? . . . 67
A-3 SABRE . . . 67
A-4 SID . . . 67
A-5 Future work . . . 69

Bibliography **71**

Glossary **75**

List of Acronyms 75

List of Symbols 76

Index **79**

List of Figures

1-1 Images of the nuclear region of the nearby galaxy NGC 7469. The left image has been obtained without AO and has a resolution of 0.7 arcsec. The right image is obtained with AO compensation and has a resolution of 0.13 arcsec. Image taken from [1]. 2

2-1 The Airy function from equation $(2\text{-}1)$ in (a) 1D and (b) 2D. 6

2-2 Schematic representation of an AO system with its main components (source: [2]). 7

2-3 The schematic representation of the scope of this thesis. The incoming phase $\varphi(k)$ at time instant k is measured by the Wavefront Sensor (WFS). With the output $s(k)$ of the WFS the reconstructed phase $\phi(k)$ can be estimated with the Wavefront Reconstruction (WFR) method. This can be used to identify the dynamics using Subspace Identification (SID). The model, represented with the system matrices $\hat{A}(k)$ and $\hat{C}(k)$, is updated at each time step. With these system matrices and $\phi(k)$, the Kalman Filter (KF) can estimate the future phase $\hat{\phi}(k+1|k)$ 9

2-4 One dimensional representation of Shack-Hartmann (SH) Wavefront Sensor (WFS) (Source: [3]). 9

2-5 Schematic representation of an Adaptive Optics system. The phase $\varphi(k)$ is aberrated due to the atmosphere, where $\xi(k)$ could be for example a zero-mean white noise sequence. The residual wavefront $\epsilon(k)$ $(2\text{-}4)$ is measured by the Wavefront Sensor (WFS), $v(k)$ denotes the measurement noise. The output of the WFS $s(k)$ is used for the Wavefront Reconstruction (WFR) to reconstruct the phase. The controller determines the input $u(k)$ of the Deformable Mirror (DM). The phase correction of the DM is denoted by $\varphi_{DM}(k)$. In this scheme it is assumed that the Subspace Identification (SID) and the Kalman Filter (KF) as shown in 2-3 are part of the controller. 11

3-1 Images of the additional known aberrations. Left: defocus for the whole image. Right: the focal plane is at a further distance than the focus distance of the lenses, so here each sub-aperture (it is a 10×10 array) has a defocus aberration. 97The aberrations are in rad. 22

3-2 Type I and type II triangulations for gradient based SABRE and intensity based SABRE for a SH WFS with 6×6 sub-apertures. The red circles show the vertices. The blue solid lines represent the edges of the triangles. The black crosses represent the centers of the sub-apertures. 24

3-3 An example of a WFR with SABRE with a SH WFS with 15×15 sub-apertures and $r_0 = 2m$ with (a) the original phase, (b) the reconstruction of the phase and (c) the absolute error between the original phase and the reconstructed phase. The units of the phase are μm. The figures (d) and (e) show the image of the SH sensor where for (e) an additional defocus aberration for each sub-aperture is applied. 25

3-4 Performance $(3\text{-}39)$ changing over time for experiment with the Fried parameter equal to $r_0 = 2m$ and a noiseless SH WFS with 15×15 sub-apertures. 26

3-5 Performance of the intensity based SABRE for a different amount of sub-apertures. The red solid line, the blue dotted line and the green dashed line represent the performance with a SH WFS with a 6×6, 8×8 and 10×10 array respectively. The x-axis shows the factor by which the unit defocus (see figure 3-1) is multiplied and the y-axis shows the performance as defined in $(3\text{-}39)$. 27

3-6 The performance versus the Fried parameter r_0 for (a) gradient based SABRE and (b) intensity based SABRE with a SH WFS without measurement noise. The legend indicate the number of sub-apertures for the corresponding SH WFS. . . . 29

3-7 The performance versus the number of sub-apertures per side for (a) gradient based SABRE and (b) intensity based SABRE with a SH WFS without measurement noise. The legend indicate the Fried parameter r_0 for the corresponding experiment. 30

3-8 The performance versus the number of sub-apertures per side for (a) gradient based SABRE and (b) intensity based SABRE with a SH WFS with measurement noise. The legend indicate the Fried parameter r_0 for the corresponding experiment 30

4-1 (a) The performance of the PO-ASID method for different values of s. (b) The performance of the APBSID method for different values of p and f. The performance is measured as a RMS of the distance between the real poles and the estimated poles of the system. 40

4-2 Eigenvalues of the estimated A matrices with PO-ASID (green circles) and APBSID (red triangles) next to the actual pole (big blue cross). The estimated poles are unbiased. 41

4-3 The eigenvalue of the (estimated) matrix $\tilde{A} = A - KC$ with APBSID (red triangles) next to the actual eigenvalue (big blue cross). 41

5-1 Triangulation and sub-domains for (a) gradient based SABRE and (b) intensity based SABRE. The black area represent the area which is not illuminated. The blue lines represent the edges of the triangles. The red circles are the vertices of these triangles. The borders of the sub-domains are shown by the green lines. The centers of the sub-apertures are represented by the black crosses. 52

5-2 Smoothed Fourier transform of different coefficients from the SABRE. The modulus is decreasing with $20dB/dec$. 54

5-3 The singular values of $W\tilde{\mathcal{O}}_f\tilde{\mathcal{K}}_pY_{0,p,N}$ (see equation $(4\text{-}29)$ in subsection 4-3-2) in decreasing order. 55

5-4 Results $(5\text{-}33)$ of the experiments for different future and past windows, denoted by f and p respectively. 55

A-1 Image of the figures produced by yao. In the top left corner the instant Point Spread Function (PSF) is shown. Below the PSF the Strehl ratio is plotted over time. The black (red) line represent the short (long) term Strehl ratio. In the left bottom corner the two DMs are shown. In this case the Stackarray and Tip-Tilt DMs are used. An image of the SH WFS is shown in the top right corner. Right bottom corner shows the residual wavefront. 66

List of Tables

3-1 Optimal amount of defocus for type I defocus and type II defocus for SH sensors with different amount of sub-apertures and the corresponding performance. . . . 27

3-2 Average performance of SABRE in combination with a SH WFS with 6×6 sub-apertures for type I and type II triangulation. 28

5-1 Results for different choices of the weighting matrix W for gradient and intensity based SABRE. 57

5-2 Comparison of the results of the CKF and the unconstrained KF. The CKF performs better than the unconstrained KF with gradient based SABRE. With intensity based SABRE using the CKF does slightly decrease the performance. 57

5-3 Results for different choices of the weighting matrix W for gradient and intensity based SABRE with PME. 58

A-1 List of parameters which needs to be defined before the initialization of the SABRE 68

A-2 List of parameters relating to Subspace Identification (SID) and Kalman Filter (KF), which can be defined before the initialization of SABRE 68

Acknowledgements

In October 2013 I resumed my Master System & Control after a year in which I built the most awesome racecar in history. Although more than a year ago, I had not forgotten the enthusiasm of Michel Verhaegen when he talked about Adaptive Optics (AO), Filtering and Identification. With that in my mind I started my graduation project with high expectations. My task: improve the estimation of the wavefront aberration by looking at the spatial dynamics and the temporal dynamics. Hence, my thesis would be about AO, Filtering and Identification!

When looking back at last year, I can say that my expectations are met. I really enjoyed last year. Sometimes I had to puzzle for days, sometimes I had to program for days, sometimes I had to dive into the literature for days. I enjoyed all single days.

The result from my last year's work is this thesis. And this would not be possible if I had not got help from many people. In the first place, I want to thank Michel Verhaegen. He motivated me with his enthusiasm and he helped me with his insights. I would also like to thank Elisabeth Brunner for giving (extensive!) feedback on my work. Also thanks to Visa Korkiakoski, who helped me with setting up the experiments with Yao, which is a major part of my project. Moreover, I would like to thank my family, for always showing great interest in my project, but also for motivating me. For all people who also helped with realization of my thesis but who are not mentioned above: thanks!

Delft, University of Technology — Erwin de Gelder
October 22, 2014

Chapter 1

Introduction

When a light beam propagates through a turbulent medium, distortions to the phase of the photon wavefront will be introduced. Adaptive Optics (AO) is a technique to actively compensate these wavefront distortions. An AO system corrects for the wavefront aberrations by measuring the aberrations with a Wavefront Sensor (WFS) and adding the estimated conjugated phase with an actuator such as a Deformable Mirror (DM). AO has several applications, such as astronomy, telecommunications, lithography and microscopy. This thesis focuses on the use of AO in astronomy.

In astronomy, AO is used to correct for the aberrations introduced by the atmospheric turbulence. Without compensation, the images obtained by ground-based telescopes are blurred, such that the angular resolution (i.e. the smallest angle between two point sources, such that they can be distinguished) is limited to about 0.5 to 1 arcsec. In figure 1-1, the increase in angular resolution is shown by two images of the galaxy NGC 7469. One image obtained without the use of AO and one image obtained with AO compensation. The image which is obtained with AO compensation is more detailed.

A crucial step in AO is the estimation of the spatial dynamics of the wavefront distortions. A WFS can only measure the intensity of light. The relation between the measured intensity and the wavefront aberration is non-linear. Hence, the estimation of the wavefront aberrations is not trivial. From the data of the WFS the wavefront needs to be reconstructed, which is the so-called Wavefront Reconstruction (WFR). The WFR is used for a real-time controller, so the WFR should be performed in the order of milliseconds [4], which is a challenge because the number of measurements is very high. Furthermore, the spatial resolution of the reconstructed wavefront must be high, so a large number of degrees of freedom is required [5].

In AO, a Shack-Hartmann (SH) WFS is commonly used. A SH WFS consists of an array of lenses with the same focal length. The deviation of the local focal spots can be used as an approximation of the local spatial derivative. Recently Visser and Verhaegen [6] proposed a new WFR method, which employed the local spatial derivatives. This method used simplex B-variate splines to model the wavefront, hence the name Spline based ABerration REconstruction (SABRE). Because of the local nature of SABRE, it is suitable for parallel programming.

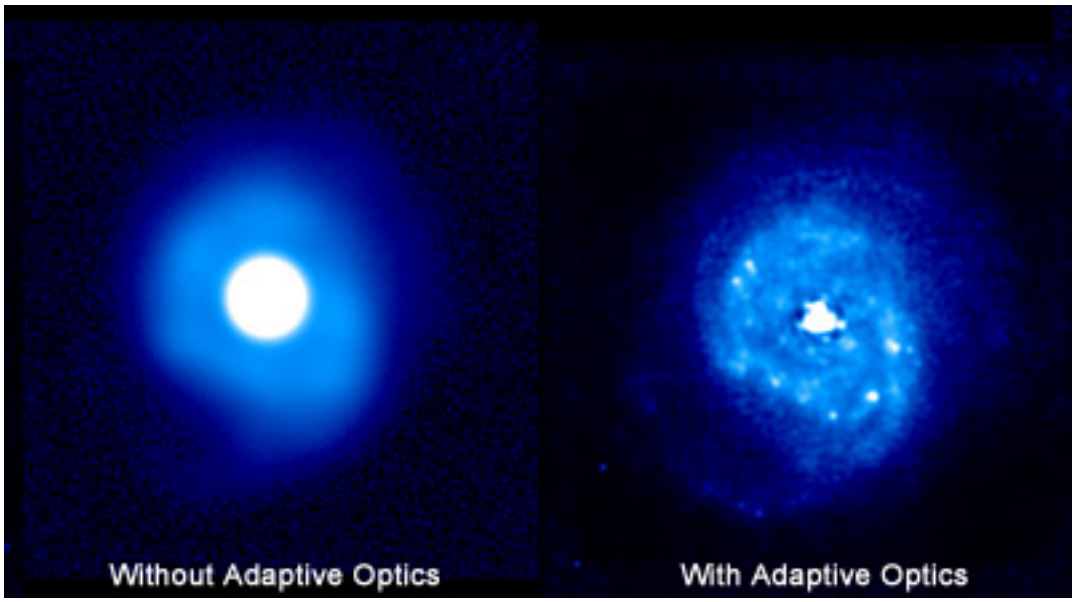

Figure 1-1: Images of the nuclear region of the nearby galaxy NGC 7469. The left image has been obtained without AO and has a resolution of 0.7 arcsec. The right image is obtained with AO compensation and has a resolution of 0.13 arcsec. Image taken from [1].

Instead of computing the local gradients, Silva et al. [7] proposed a linear procedure used to reconstruct a wavefront directly from the intensities using SABRE with a Hartmann sensor. The Hartmann sensor differs from the SH sensor as it consists of an array of apertures instead of an array of lenses. Intensity based SABRE refers to the fact that SABRE is used in combination with the intensity measurements. Intensity based SABRE can increase the performance significantly, because the intensity patterns contains more information than the estimated spatial derivatives. In order to have an applicable method for AO, this method is adopted for the SH WFS. With AO simulations with Yao, it is demonstrated that the intensity based SABRE provides good estimates of the wavefront aberrations under some conditions. With the simulations, intensity based SABRE is compared with gradient based SABRE.

Due to the read-out time of the WFS process and the computations of the WFR, a delay is introduced. Hence, it is useful to not only reconstruct the wavefront from the WFS data, but also to predict the future wavefront, such that the temporal dynamics are taken into account. For this purpose a Kalman Filter (KF) is applied. The KF is adapted, such that it applicable in combination with SABRE. Moreover, the local nature of SABRE is exploited, such that the KF is very suitable for parallel programming. We will present how Alternating Direction Method of Multipliers (ADMM) [8] can be exploited for the KF.

The KF needs to know how the system behaves, e.g. a description of the temporal dynamics. A model is obtained with Subspace Identification (SID). The SID is adapted to a method which is compliant with the local nature of SABRE. Hence, the SID method can also be performed in a distributive manner.

The performance of the SID and the KF is examined with AO simulations with Yao. It is described how the most important parameters are chosen or tuned. The experiments

demonstrate that the KF predicts the aberration significantly more accurate compared to the delayed reconstruction and at times even outperforms the reconstruction without delay.

1-1 Problem statement

The goal of this project is to show that intensity based SABRE performs better than the traditional method, which uses slope measurements, when used to reconstruct the wavefront in real-time where a Shack-Hartmann sensor is used as WFS. Furthermore, it should be demonstrated that with SID and a KF the performance can be even further improved by compensating for the delay introduced by the WFS and WFR.

1-2 Thesis layout

The structure of this thesis is as follows. Some theoretical background of AO is presented in chapter 2. Based on the problem statement the research can be divided into three parts: SABRE, SID and KF. Chapter 3 introduces SABRE and gradient based SABRE will be compared with intensity based SABRE. In chapter 4, two Autonomous Subspace Identification (ASID) methods will be presented and applied to a fictive system. The KF will be explained in chapter 5. In an experiment it will be demonstrated that with a KF in combination with SID the prediction of the wavefront can be improved by compensating for the delay. Chapter 6 concludes this thesis and provides recommendations for further research.

Chapter 2

Motivation

As mentioned in the introduction of this thesis, the focus will be on the estimation of the wavefront with the spatial and temporal dynamics taken into account. Spline based ABerration REconstruction (SABRE) will be used for the Wavefront Reconstruction (WFR). Furthermore, Subspace Identification (SID) and a Kalman Filter (KF) will be used for the filtering of the SABRE. This chapter provides a motivation for SABRE to model the spatial dynamics. Besides, the motivation for SID and the KF to model and to correct for the temporal dynamics is provided. In order to motivate the choices, some important aspects of Adaptive Optics (AO) will be described.

In section 2-1, it will be explained why AO can increase the image resolution of ground-based telescopes. Section 2-2 presents how an AO system works in general. The goal of AO is to increase the image resolution as much as possible. However, the resolution depends non-linear on the wavefront. Therefore another control objective is provided in section 2-3. As already mentioned, the focus of this thesis is on the WFR and its filtering, which is discussed in section 2-4.

2-1 The need for Adaptive Optics

Let us assume that we have an ideal ground based telescope, meaning that it is not affected by atmospheric turbulence. Then the image of a point source (star) can be described by an Airy function:

$$p_0(\alpha) = \frac{\pi D^2}{4\lambda^2} \left(\frac{2J_1(\pi D|\alpha|/\lambda)}{\pi D|\alpha|/\lambda} \right)^2. \tag{2-1}$$

Here, $p_0(\alpha)$ is the measured intensity at angular coordinate α. The diameter is denoted by D, λ denotes the wavelength of light and $J_1(\cdot)$ is the Bessel function of the first kind. The intensity p_0 is shown in figure 2-1 for both the 1D and 2D case.

If two point sources are too close to each other, then they can not be distinguished due to the diffraction caused by the finite diameter of the telescope. The Rayleigh criterion states that

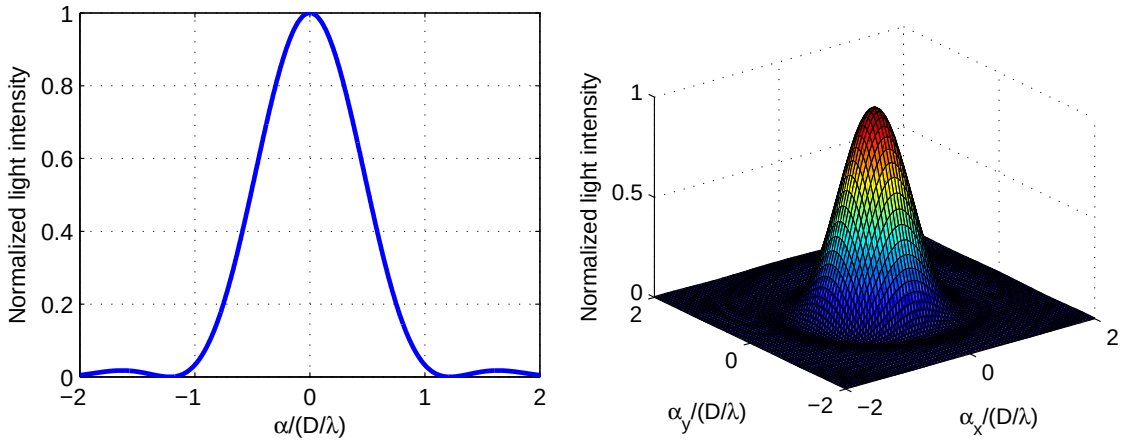

(a) 1D case **(b)** 2D case

Figure 2-1: The Airy function from equation (2-1) in (a) 1D and (b) 2D.

two points cannot be distinguished if the center of the Airy disc for the first point occurs at the first minimum of the Airy disk of the second point. The first dark ring is at an angular distance of

$$\alpha = 1.22\lambda/D. \tag{2-2}$$

Hence, the angular resolution is diffraction limited due to the finite diameter D. This motivates us to build larger telescopes. However, if the telescope gets larger, then the atmospheric turbulence will become a limiting factor and (2-2) does not hold anymore. To further improve the imaging quality of large ground-based telescopes it is necessary to reduce the disadvantageous effect of the atmospheric wavefront aberrations on the imaging process. This is the task of an Adaptive Optics (AO) system [2].

2-2 Principle of adaptive optics

In order to explain the principle of AO, consider figure 2-2. When the light of a star enters the atmosphere, it has a plane wavefront, i.e. the wavefront is undisturbed. Due to atmospheric turbulence the wavefront will be disturbed when it reaches the telescope. The disturbances introduce time and space varying optical path length differences. This gives rise to a turbulence induced phase profile, simply called disturbed wavefront. It is generally assumed that the amplitude is not disturbed by the atmospheric turbulence. The wavefront is denoted by $\psi(r,t)$, where r denotes the spatial coordinate and k denotes the time. The wavefront is given by

$$\psi(r,k) = Ae^{i\varphi(r,k)}, \tag{2-3}$$

where $\varphi(r,k)$ denotes the phase and A represents the amplitude. Since the aberrations only affect the phase it is assumed that $A = 1$.

The AO system corrects for the disturbed wavefront with an actuator, which is typically a Deformable Mirror (DM). After the phase correction $\varphi_{DM}(r,k)$ introduced by the DM, there

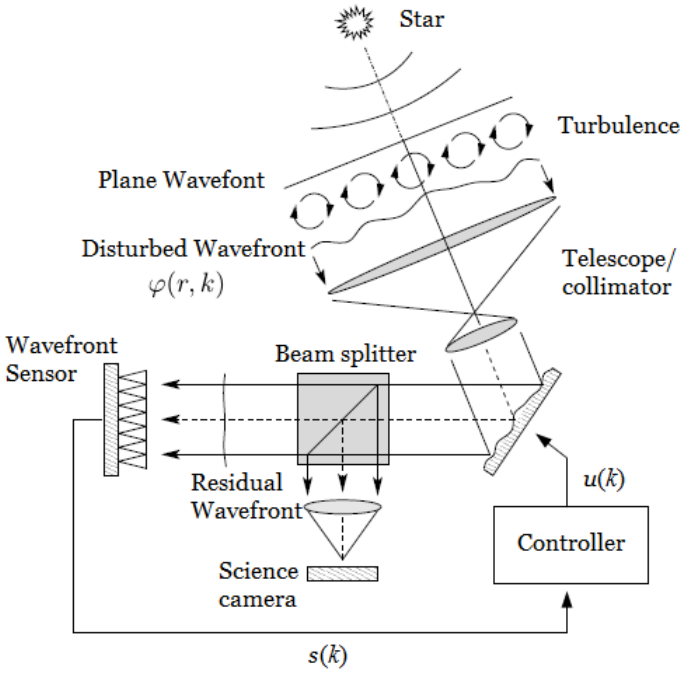

Figure 2-2: Schematic representation of an AO system with its main components (source: [2]).

is a residual phase error:

$$\epsilon(r,k) := \varphi(r,k) - \varphi_{DM}(r,k). \tag{2-4}$$

After this, a beam splitter divides the light into two parts. One part goes to the science camera which will make an image of the light for scientific purposes. The other part of the light is directed to the Wavefront Sensor (WFS). The WFS measurements $s(k)$ are sent to the controller, which has to determine an input $u(k)$ for the actuators.

2-3 Control objective of adaptive optics

The measured intensity from an object is a smoothed version of the object itself. For the ideal telescope without atmosphere, the intensity is given by the convolution of the Airy function of (2-1) and the object $o(\alpha)$:

$$i(\alpha) = \iint o(\beta)p_0(\alpha - \beta)d\beta.$$

Here, $p_0(\alpha)$ (2-1) is a so-called Point Spread Function (PSF). This is the ideal PSF because the phase aberrations φ equal zero. If also atmospheric turbulence is taken into account (i.e. $\varphi \neq 0$), then the image of a point source will be different. Let in general the PSF be denoted by $p(\alpha)$. The ultimate goal of AO is to achieve that the PSF $p(\alpha)$ equals $p_0(\alpha)$ from (2-1). It is common in AO to define the objective of AO with the Strehl ratio. The Strehl ratio S is defined as the ratio of the peak intensity from the PSF and the Airy function $p_0(\alpha)$:

$$S := \frac{p(0)}{p_0(0)}. \tag{2-5}$$

The maximum value of the Strehl ratio is 1. The objective of AO is to maximize the Strehl ratio. However, the relation to the residual wavefront ϵ and the Strehl ratio is non-linear, which makes it difficult to have this as an objective. Therefore Maréchal's approximation is widely used:

$$S(\sigma_\epsilon) \approx e^{-(2\pi\sigma_\epsilon)^2}.$$

With this approximation the Strehl ratio is strictly decreasing with an increasing variance σ_ϵ^2 of the residual wavefront ϵ. Hence, instead of maximizing the Strehl ratio of (2-5), the objective of AO is to minimize the variance of the residual wavefront ϵ. Although Maréchal's approximation is only valid with certain assumptions it is shown that minimizing σ_ϵ^2 indeed leads to the maximum Strehl ratio [9, 10].

2-4 Scope of the thesis

As explained in section 2-2 a controller has to determine the input $u(k)$ based on the measurements $s(k)$ from the WFS. A classical approach is to determine the input using an interaction matrix. The interaction matrix maps the input of the DM to the output of the WFS. There are several techniques to compute or estimate this interaction matrix [11]. The input of the DM can be computed by multiplying the pseudo inverse of the interaction matrix with the WFS output vector. An advantage of this method is its simplicity: only a matrix-vector multiplication is required. It might be a challenge to compute the pseudo inverse of the interaction matrix, but this can be done off-line.

Unfortunately, there are also some disadvantages of the aforementioned method. When the number of actuators is large, the interaction matrix can be ill-conditioned [12]. Hence, the input of the DM can be highly sensitive to small errors of the WFS measurements or small errors in the knowledge of the interaction matrix, due to uncertainty or temporal variations. Another disadvantage is the assumption of a static system. For example, the read-out time of the sensors introduce a delay. Also the computations contribute to the delay, so the assumption of a static system is not true.

These disadvantages motivate another approach. Instead of computing the DM commands directly from the inputs a few extra steps are used. The first step is to estimate the wavefront phase $\varphi(k)$ from the WFS data $s(k)$. This step is called the Wavefront Reconstruction (WFR). The estimated phase, denoted by $\phi(k)$, will be used to compute the optimal DM shape $\phi_{DM}(k)$. The last step is to compute the inputs $u(k)$ such that the DM shape is as close to $\phi_{DM}(k)$ as possible.

In this thesis, the focus will be on the WFR and its identification and filtering. In figure 2-3 the scope of the thesis is shown schematically. The objective of the WFR is to estimate the phase $\phi(k)$. However, since the WFS need some time to produce the measurements, the data $s(k)$ is already 'outdated'. Also the WFR requires some time, so $\phi(k)$ is even more 'outdated'. Therefore it is useful to estimate the future phase. This estimate is denoted by $\hat{\phi}(k+1|k)$. The index $(k+1|k)$ means that the phase at time instant $k+1$ is estimated using data up to time instant k. The estimate $\hat{\phi}(k+1|k)$ can be computed with a Kalman Filter (KF) [13]. The KF needs to know how the system behaves, e.g. with a state space description. Therefore Subspace Identification (SID) is used. These three aspects, WFR, SID and KF will be treated in the thesis. In the following subsections the contributions to the WFR, SID and KF will be explained individually.

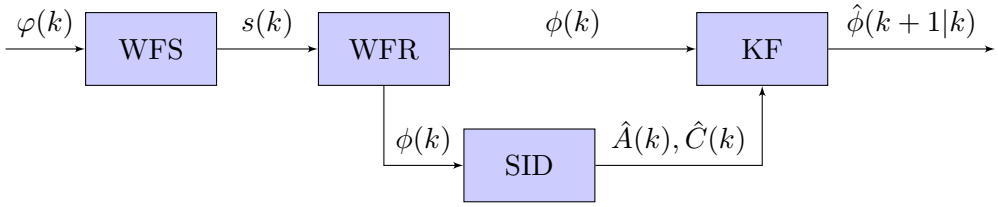

Figure 2-3: The schematic representation of the scope of this thesis. The incoming phase $\varphi(k)$ at time instant k is measured by the Wavefront Sensor (WFS). With the output $s(k)$ of the WFS the reconstructed phase $\phi(k)$ can be estimated with the Wavefront Reconstruction (WFR) method. This can be used to identify the dynamics using Subspace Identification (SID). The model, represented with the system matrices $\hat{A}(k)$ and $\hat{C}(k)$, is updated at each time step. With these system matrices and $\phi(k)$, the Kalman Filter (KF) can estimate the future phase $\hat{\phi}(k+1|k)$

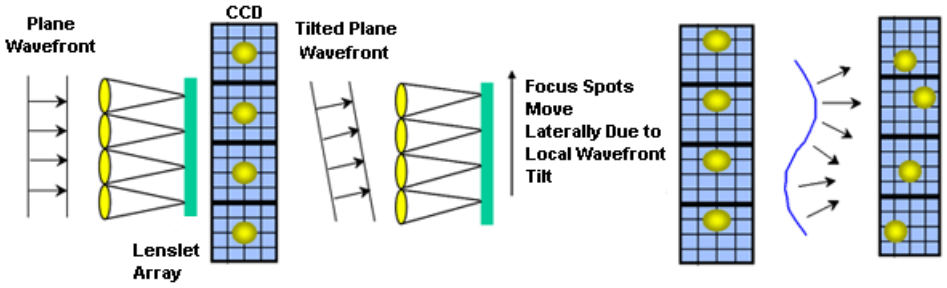

Figure 2-4: One dimensional representation of Shack-Hartmann (SH) Wavefront Sensor (WFS) (Source: [3]).

2-4-1 Wavefront Reconstruction

The wavefront cannot be measured directly because it is only possible to measure intensities and the relation between the intensities and the wavefront is non-linear. Therefore, it is not trivial to reconstruct the wavefront from the sensor data. A widely used sensor which is used for the WFR, is a Shack-Hartmann (SH) sensor [14]. It is assumed throughout this thesis that the WFS is a SH sensor, although the results are extendable to other sensors.

The SH WFS consists of an array of lenses with same focal length. The deviation of the local focus spots can be used as an approximation of the local spatial derivative. With the use of a centroid algorithm, this sensor can provide these local spatial slopes of the phase aberration. These slopes are approximated by the center of mass of the intensity distribution in the detector. There are many methods that reconstruct the wavefront from the slope data. One of these methods is the so-called Spline based ABerration REconstruction (SABRE) [6]. In this thesis SABRE is used for the WFR. There are several advantages of SABRE [6]:

- SABRE is invariant for different WFS geometries. For many methods a rectangular grid is required, which e.g. limits the design of the WFS. Also with SABRE misalignment of the WFS does not have to result in biased results.
- SABRE uses simplex B-variate splines which can be of any degree, so non-linear basis functions can be used as well.

- SABRE is insensitive to sensor noise compared to the conventional WFR methods that make use of slope measurements.
- In contrast to the Fried method SABRE is not subject to the waffle mode [15].
- SABRE has the potential to be solved in a distributive manner, which increases the computational efficiency [16].

Because SABRE is a promising WFR method, it will be used in this thesis. The aforementioned method uses estimated spatial gradients. We will refer to it as gradient based SABRE.

SABRE can also be used when the measured intensities are used directly, so without using the centroids. This will be called intensity based SABRE. In [7] it is shown that intensity based SABRE gives good results when the aberrations are small. In this thesis this method is adopted for a SH sensor.

The performance of the gradient and the intensity based SABRE will be compared when used for reconstruction of aberrations. These aberrations are modeled using the Kolmogorov model [17], such that it represents wavefront aberrations resulting from light which has traveled through the atmosphere.

2-4-2 Subspace Identification

There exist many methods for identification of a system, but in this thesis only Subspace Identification (SID) is considered. The main advantages of SID compared to other identification techniques, are the following:

- With SID, the identified model does not need to be parameterized before identification. Other methods, like the output-error and prediction-error methods, need a model structure and the amount of poles and zeros (depending on the model structure that is chosen). As there is little information known about the wavefront aberrations, it is difficult to have information about the model structure. Note that although with SID no parameterized model is needed, the order n of a system needs to be known while calculating the system matrices. Fortunately, with the singular values of the Singular Value Decomposition (SVD) that will be computed, good estimates can be calculated under fairly minor conditions [18].
- The main steps of SID are an RQ factorization, an Singular Value Decomposition (SVD) and a solution to a linear least squares problem. These are all linear-algebra steps, so there is no need for a non-linear optimization. A non-linear optimization can give problems with local minima, such that a good initial estimate is needed. Since the wavefront aberrations are difficult to model, it is very difficult to come up with a good initial estimate. Furthermore the speed of a non-linear optimization depends on the convergence of the problem, which can differ from one time to the other. Hence, the fact that the key steps of SID consist of linear-algebra makes it advantageous when it is applied to AO.
- SID is suitable for systems with more than one input and/or more than one output. Later it will be shown that this is an advantage in this application.

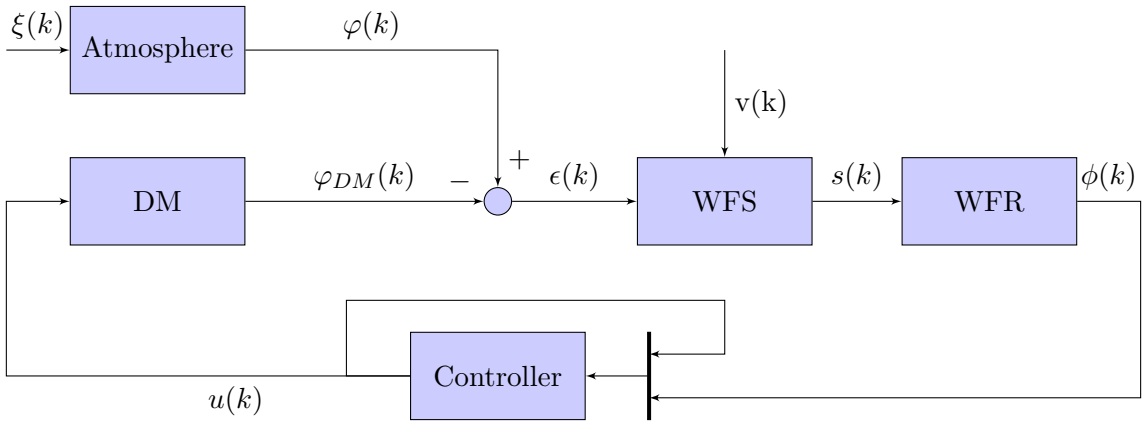

Figure 2-5: Schematic representation of an Adaptive Optics system. The phase $\varphi(k)$ is aberrated due to the atmosphere, where $\xi(k)$ could be for example a zero-mean white noise sequence. The residual wavefront $\epsilon(k)$ (2-4) is measured by the Wavefront Sensor (WFS), $v(k)$ denotes the measurement noise. The output of the WFS $s(k)$ is used for the Wavefront Reconstruction (WFR) to reconstruct the phase. The controller determines the input $u(k)$ of the Deformable Mirror (DM). The phase correction of the DM is denoted by $\varphi_{DM}(k)$. In this scheme it is assumed that the Subspace Identification (SID) and the Kalman Filter (KF) as shown in 2-3 are part of the controller.

- It is possible to implement SID in a recursive manner, which makes it suitable for real-time identification.

The output of the WFR will be used for the identification. In figure 2-5 a scheme of an AO system is shown. If intensity based SABRE is used, then the output of the WFS represents the measured intensities. This is in general a large amount of data, as there are many more pixels in the detector than slope measurements. Therefore the output of the WFR will be used for identification. In figure 2-5 the output of the WFR is denote by $\phi(k)$.

As can be seen in figure 2-5 the system is operating in closed loop. There are SID methods that give unbiased results, even when the system is operating in closed loop. However, these methods require the reference signal to be persistently exciting. This is not the case, because the reference is always a flat wavefront. Therefore this thesis focuses on open loop identification with the input $u(k) = 0$. Hence, we are dealing with Autonomous Subspace Identification (ASID).

With ASID the dynamics of the wavefront aberrations can be estimated. However, these dynamics are also changing in time. Hence, the estimated model should be updated at each time step and Recursive Autonomous Subspace Identification (RASID) can be used.

Although ASID will be used it can still be useful when used in the closed loop case. The reconstructed phase can be separated into two parts:

$$\phi(k) = \phi_{\text{atmosphere}}(k) - \phi_{DM}(k).$$

Here $\phi_{DM}(k)$ represents the reconstructed correction of the DM and $\phi_{\text{atmosphere}}(k)$ is the reconstructed aberration $\varphi(k)$. The reconstructed phase correction $\phi_{DM}(k)$ only depend

on the input of the DM $u(k)$. It is possible to identify the system which models $\phi_{DM}(k)$ as a function of $u(k)$ [11]. That implies that with the known $u(k)$ the reconstructed phase correction $\phi_{DM}(k)$ can be computed, so $\phi_{\text{atmosphere}}(k)$ can be computed as well. Although the system is operating in closed loop, (R)ASID can still be used with the data of $\phi_{\text{atmosphere}}(k)$.

2-4-3 Kalman Filtering

In literature, many filters are proposed. In this thesis, only a KF is considered, because of the following properties:

- It is a linear filter. Because of the speed at which the filtering should be performed, a filter that does not need non-linear optimization is highly preferred.
- The KF is the minimum-variance state estimator for linear dynamic systems with Gaussian noise [19]. The system is estimated using SID, which estimates a linear system. Hence, it makes sense to assume that the system is linear.
- The KF is the minimum-variance linear state estimator for linear dynamic systems with non-Gaussian noise [20]. The noise of the system is unknown, but although the noise may be non-Gaussian, the KF is still the optimal linear filter. As mentioned earlier, a linear filter is preferred.

The goal of the Kalman Filter (KF) is to predict the phase one time instant in the future, i.e. $\varphi(k+1)$ has to be predicted with data up to time instant k. In general, the prediction - denoted by $\phi(k+1|k)$ - contains much information, so the time which is required for the computation of $\phi(k+1|k)$ becomes an issue. Because the KF is used in real-time, it will be presented how the KF can be implemented such that many computations can be done in a distributive manner.

As mentioned earlier, SABRE has the potential to be solved in a distributive manner. This is a result from the fact that the splines are defined locally, so the SID and KF can also be implemented locally, and thus in a distributive manner. In order to ensure a certain order of continuity the locally defined splines are subject to some constraints. The KF has to handle these constraints as well, so a Constrained Kalman Filter (CKF) will be used. It will be shown how the CKF can be implemented in a distributive manner with the Alternating Direction Method of Multipliers (ADMM).

Chapter 3

Wavefront Reconstruction with SABRE

3-1 Introduction

In Adaptive Optics (AO) the resolution of an image is improved by correcting the wavefront aberrations. In for example ground-based telescopes, light propagates through a medium that has an inhomogeneous refractive index which leads to a modification in the shape of the phase. Typically a Deformable Mirror (DM) is used to correct for these aberrated wavefronts. A crucial step in an AO system is to measure the wavefront with enough spatial resolution and speed to apply the real-time correction [5].

The wavefront cannot be measured directly as only intensities can be measured. Hence, a Wavefront Reconstruction (WFR) method is required to reconstruct the phase from the measurements. In many applications, for example in astronomy, the WFR is used for a real-time controller, so the WFR should be done in the order of milliseconds [4]. The spatial resolution requirement of adaptive optics wavefront sensors is usually very high, so a large number of degrees of freedom is required [5].

In this chapter two different WFR methods will be compared. Both methods use data from a Shack-Hartmann (SH) Wavefront Sensor (WFS) [14]. The SH WFS consists of an array of lenses with the same focal length. Each lens is focused on a photon sensor, which is commonly a Charge-Coupled Device (CCD) array. The photon sensor measures the intensity of the light beam. The relation between the measured intensities and the wavefront is non-linear. However, the deviation of the focal spot gives an approximation of the local spatial derivative. The deviation of the focal spot can be computed using a centroid algorithm. One method uses the intensity measurements, while the other method uses the estimated local slopes.

Both methods are based on a method called Spline based ABerration REconstruction (SABRE), which is proposed by Visser and Verhaegen [6]. With SABRE the phase is modeled with bi-variate simplex B-splines [21]. Visser and Verhaegen use the slope measurements from a

Shack Hartmann (SH) sensor to reconstruct the wavefront [6]. Another method, proposed by Silva et al. [7], makes use of the whole intensity pattern. The relation between the measured intensities and the wavefront is highly non-linear which will result in many local minima [22]. Furthermore, when making use of one image the solution is non-unique [23]. However, by linearizing the intensity with respect to the optimization variables, Silva et al. [7] show that a fast unique solution can be provided. By using the intensity pattern rather then only the centroids of the spots, also higher order aberrations can be taken into account, because the centroids only give information about the local tip and tilt aberrations.

The outline of this chapter is as follows. In section 3-2, some WFR principles are discussed. In section 3-3, SABRE is explained. Here it is also summarized how slope measurements or intensity measurements are used to estimate the wavefront. The experiments in which both previously described methods are compared, is represented in section 3-4. This chapter ends with a conclusion in section 3-5.

3-2 Wavefront Reconstruction principles

3-2-1 Optical Image Formation

The wavefront is given by equation 2-3 as

$$\psi(r,t) = Ae^{i\varphi(r,t)}. \tag{3-1}$$

The complex amplitude Z of a wave ψ diffracting through an aperture P is given by Huygens' principle, which states that each point in the aperture can be considered as the center of an emerging spherical wave. In the far field (i.e., in the case of Fraunhofer diffraction), the spherical waves are equivalent to plane waves, and the expression for the amplitude as a function of position α in the focal plane can be written as follows [24]:

$$Z(\alpha) = \frac{1}{\sqrt{\Pi}} \int \psi(r)P(r)e^{\frac{-2\pi i\alpha r}{\lambda}} du. \tag{3-2}$$

Here, $P(r)$ is the aperture, which is for a fully transmissible and aberration free case $P(r) \equiv 1$ for r inside the aperture and $P(r) \equiv 0$ for r outside the aperture. Π is the total area of P, λ is the wavelength of the photons and α denotes the position in the focal plane. Note that if the diffracted light is focused with a lens, the observed diffraction pattern can be modeled using Fraunhofer diffraction [25]. With the introduction of $u = r/\lambda$, equation (3-2) can be rewritten as a Fourier transform [24]:

$$Z(\alpha) = \frac{1}{\sqrt{\Pi}} \mathcal{F}\left[\psi(u)P(u)\right].$$

Here $\mathcal{F}[\cdot]$ denotes the Fourier transform of $(\cdot)$. Image sensors only measure the intensity, which is given by the square of the amplitude of the signal:

$$I(\alpha) = |Z(\alpha)|^2 = \frac{1}{\Pi} \left|\mathcal{F}\left[\psi(u)P(u)\right]\right|^2.$$

Together with (3-1) the intensity, denoted by I, becomes

$$I(\alpha) = \frac{1}{\Pi} \left|\mathcal{F}\left[Ae^{i\varphi(u)}P(u)\right]\right|^2. \tag{3-3}$$

3-2-2 Different methods for Wavefront Reconstruction

The goal of WFR is to reconstruct the phase, denoted by $\varphi(r)$. The reconstructed phase is denoted by $\phi(r)$. The time dependency is omitted for brevity. In this chapter, the difference between the phase and its reconstruction is called the residual phase. There are two major classes to reconstruct the wavefront: the focal plane sensor and the pupil plane sensor.

Pupil plane sensors

With pupil plane sensors, the slope of the phase is measured. The relation between the slopes $\sigma_x(x,y)$ and $\sigma_y(x,y)$ of the phase $\varphi(x,y)$ at the spatial coordinates x and y can be described by first order partial differential equations:

$$\sigma_x(x,y) = \frac{\partial\varphi(x,y)}{\partial x}, \tag{3-4}$$

$$\sigma_y(x,y) = \frac{\partial\varphi(x,y)}{\partial y}. \tag{3-5}$$

The SH sensor is currently the most widely used sensor for AO due to its simplicity and reliability. With the deviation of the focal spot with respect to the center, the local tilt can be calculated:

$$\begin{aligned}\Delta x(i,j) &= \kappa_x \frac{\partial\phi(x_i,y_j)}{\partial x} + \eta_x(i,j) = \kappa_x\sigma_x(x_i,y_i) + \eta_x(i,j),\\ \Delta y(i,j) &= \kappa_y \frac{\partial\phi(x_i,y_j)}{\partial y} + \eta_y(i,j) = \kappa_y\sigma_y(x_i,y_i) + \eta_y(i,j).\end{aligned}$$

The location of the focal spot with respect to the center is given by $\Delta x(i,j)$ and $\Delta y(i,j)$ where i,j denotes the lens in the i-th row and j-th column. The constants κ_x and κ_y are determined by the optical parameters of the system. $\eta_x(i,j)$ and $\eta_y(i,j)$ represent the measurement noise and the effect from higher order aberrations, i.e. aberrations that differ from piston, tip and tilt. With a CCD the location of the focal spot is usually measured with the centroid algorithm [26, 27], which computes the centers of mass of the intensity distribution (3-3) in the detector. Let U and V be the amount of columns and rows of pixels for each aperture or lens. If the x-location and y-location with respect to the center $(x(i), y(j))$ is given by $X(u)$ and $Y(v)$ respectively, with $u \in \{1,2,\ldots,U\}$ and $v \in \{1,2,\ldots,V\}$, then the centroid algorithm can be formulated as follows:

$$\Delta x(i,j) = \frac{\sum_{u=1}^{U}\sum_{v=1}^{V} X(u)I(x(i)+X(u), y(j)+Y(v))}{\sum_{u=1}^{U}\sum_{v=1}^{V} I(x(i)+X(u), y(j)+Y(v))} \tag{3-6}$$

$$\Delta y(i,j) = \frac{\sum_{u=1}^{U}\sum_{v=1}^{V} Y(u)I(x(i)+X(u), y(j)+Y(v))}{\sum_{u=1}^{U}\sum_{v=1}^{V} I(x(i)+X(u), y(j)+Y(v))}. \tag{3-7}$$

Other sensors that provide spatial derivative measurements are the pyramid [28] and curvature [29] sensors. In this thesis it is assumed that the WFR sensor is a SH sensor, although the results may be extendable to other sensors.

Pupil plane sensors are also called *gradient based* sensors. Although it uses intensity sensors, it calculates an approximation of the slopes of the wavefront. The slopes will be used for the reconstruction of the wavefront and hence, these sensors are called gradient based.

Pupil plane sensors use either modal or zonal measurements [30]. With modal sensing the idea is to decompose the wavefront into a number of distinct surface shapes. In most cases, each surface shape or mode is represented by a Zernike polynomial [31]. Modal measurements are well suited if lower order aberrations are dominant. With zonal measurements the wavefront is decomposed into smaller zones (see for example [32]). For each zone a wavefront is reconstructed. The number of zones is such that low order aberrations are dominant within one zone. These type of measurements are better suited than modal measurements if higher order aberrations are dominant [5].

Well known approximations of the derivatives are proposed by Fried [32], Hudgin [33] and Southwell [34]. Although these methods are simple - they only use local tilts - there are algorithms developed recently that can handle these reconstruction very efficiently [35, 36, 37]. Recently Visser and Verhaegen proposed a WFR method, called Spline Based Aberrations Reconstruction (SABRE) [6]. With SABRE, the wavefront is locally modeled with simplex B-splines instead of local tilts. See subsection 3-3-2 for an explanation of SABRE with gradient measurements.

Focal plane sensors

The focal plane sensors use the intensity measurements obtained via a CCD. The measured image could be from a SH sensor, but other sensors are not excluded. The main advantage of using the whole image is the fact that no information is lost. With pupil plane sensors, only the slopes are considered. A disadvantage is the fact that the relation between the to be reconstructed phase and the measured intensity pattern is non-linear.

Polo et al. proposed a focal plane method in combination with a Hartmann sensor [38]. The phase is modeled as a weighted sum of Zernike modes. A non-linear iterative solver is used to compute the estimated weights. Simulations show that the root mean square of the difference between the real wavefront and the estimated wavefront decreases by an order of magnitude with respect to the traditional wavefront reconstruction based on the wavefront slope measurement.

Although there are working focal plane sensors, this approach is considered to be not very well suited for WFR. Firstly the method is computationally complex, which is not desirable for real-time systems [39]. Secondly, because of the high non-linearities there are many local minima [22]. The reconstruction requires many degrees of freedom, so this property makes these sensors unreliable. However, as we will see in section 3-3-3, after linearizing the modeled intensities with respect to the optimization variables the problem becomes linear. In that case, focal plane sensors can be used for real-time WFR.

3-3 Spline Based Aberration Reconstruction

3-3-1 Bivariate simplex B-splines

Here follows a brief description of Spline based ABerration REconstruction (SABRE). This subsection is based on the work of Visser and Verhaegen [6] to which I refer the reader for a more detailed description.

The wavefront domain will be partitioned into J non-overlapping simplices, which in this case are triangles. The triangulation domain is denoted by $\mathcal{T}$. Each triangle t is formed by the convex hull of its three non-degenerate vertices $v_0, v_1, v_2 \in \mathbb{R}^2$. The splines are represented in Barycentric coordinates, which are local variables defined on an individual triangle. The cartesian coordinates $x \in \mathbb{R}^2$ are related to the Barycentric coordinates $b \in \mathbb{R}^3$ in the following way:

$$x = \begin{bmatrix} v_0 & v_1 & v_2 \end{bmatrix} b. \tag{3-8}$$

In the remainder of this section, the following shorthand notation will be used:

$$b(x) := (b_0, b_1, b_2) \in \mathbb{R}^3,\ x \in \mathbb{R}^2,\ b_0 + b_1 + b_2 = 1. \tag{3-9}$$

On a simplex the local basis is formed by the Bernstein polynomials in terms of the Barycentric coordinates. These polynomials of degree d can be expanded into monomials, with the following property:

$$(b_0 + b_1 + b_2)^d = \sum_{\|\kappa\|_1 = d} \frac{d!}{\kappa_0!\kappa_1!\kappa_2!} b_0^{\kappa_0} b_1^{\kappa_1} b_2^{\kappa_2}, \tag{3-10}$$

with $\kappa = (\kappa_0, \kappa_1, \kappa_2)$ a multi-index with the properties

$$\|\kappa\|_1 = \kappa_0 + \kappa_1 + \kappa_2 = d, \kappa_0 \geq 0, \kappa_1 \geq 0, \kappa_2 \geq 0. \tag{3-11}$$

The Bernstein basis polynomials of the simplex B-splines are defined as the individual monomials in (3-10), with the additional rule that they are equal to 0 by definition when the evaluation point x is outside of the triangle t:

$$B_\kappa^d(b(x)) := \begin{cases} \frac{d!}{\kappa_0!\kappa_1!\kappa_2!} b_0^{\kappa_0} b_1^{\kappa_1} b_2^{\kappa_2} & \text{if } x \in t \\ 0 & \text{if } x \notin t \end{cases} \tag{3-12}$$

A linear combination of the Bernstein basis polynomials gives then the B-form polynomial:

$$p_t(b(x)) := \begin{cases} \sum_{\|\kappa\|_1 = d} c_\kappa^t B_k^d(b(x)) & \text{if } x \in t \\ 0 & \text{if } x \notin t \end{cases} \tag{3-13}$$

Here c_κ^t are the B-coefficients which uniquely determine the polynomial $p(b(x))$ on the triangle t. Equation (3-13) can also be written in vector notation:

$$p_t(b(x)) := \begin{cases} \mathbf{B}_t^d(b(x)) \cdot c^t & \text{if } x \in t \\ 0 & \text{if } x \notin t \end{cases} \tag{3-14}$$

All the monomials in $\mathbf{B}_t^d(b(x)) \in \mathbb{R}^{1 \times \hat{d}}$ and constants in $c^t \in \mathbb{R}^{\hat{d} \times 1}$ with $\hat{d} = \frac{(d+2)!}{2d!}$ are sorted lexicographically according to [40]:

$$\mathbf{B}_t^d(b(x)) := \begin{bmatrix} B_{d,0,0}^d(b(x)) & B_{d-1,1,0}^d(b(x)) & \cdots & B_{0,0,d}^d(b(x)) \end{bmatrix}, \tag{3-15}$$

$$c^t := \begin{bmatrix} c^t_{d,0,0} & c^t_{d-1,1,0} & \cdots & c^t_{0,1,d-1} & c^t_{0,0,d} \end{bmatrix}^T. \tag{3-16}$$

The simplex B-spline funtion $s^r_d(b(x))$ of degree d and continuity order r (also denoted by C^r) can be defined on a triangulation $\mathcal{T}_J$ consisting of J triangles:

$$s^r_d(b(x)) := \mathbf{B}^d \cdot c \in \mathbb{R}, x \in \mathcal{T}_J. \tag{3-17}$$

Here $\mathbf{B}^d$ and c are constructed using respectively (3-15) and (3-16):

$$\mathbf{B}^d := \begin{bmatrix} \mathbf{B}^d_{t_1}(b(x)) & \mathbf{B}^d_{t_2}(b(x)) & \cdots & \mathbf{B}^d_{t_J}(b(x)) \end{bmatrix} \in \mathbb{R}^{1 \times J\hat{d}} \tag{3-18}$$

$$c := \begin{bmatrix} {c^{t_1}}^T & {c^{t_2}}^T & \cdots & {c^{t_J}}^T \end{bmatrix}^T \in \mathbb{R}^{J\hat{d} \times 1} \tag{3-19}$$

The goal of the WFR is to compute the vector of coefficients c. Estimates of the wavefront can be obtained at any desired location in the triangulation by evaluating the spline function (3-17).

Because splines are used one can enforce a certain continuity of order r, such that all m-th order derivatives, with $0 \leq m \leq r$ of two neighboring triangles are equal on the edge between the two triangles. All the continuity conditions give a single set of linear equations:

$$Ac = 0. \tag{3-20}$$

Here A is the so-called smoothness matrix. How to construct A is described in [41].

3-3-2 SABRE with gradient measurements

The goal of SABRE is to reconstruct the wavefront using bivariate simplex B-splines. Therefore it is assumed that the unknown wavefront $\varphi(x, y)$ can be approximated with the bivariate simplex B-spline from (3-17):

$$\varphi(x, y) \approx \phi(x, y) = s^d_r(b(x, y)) = \mathbf{B}^d(b(x, y)) \cdot c, d \geq 1, (x, y) \in \mathcal{T}_J.$$

Under the assumption that this equation holds, then using (3-4) and (3-5) the slope sensor model becomes:

$$\sigma_x(x, y) = \frac{d!}{(d-1)!}\mathbf{B}^{d-1}(b(x, y))P^{d,d-1}(a_x) \cdot c^t + \eta_x(x, y), \tag{3-21}$$

$$\sigma_y(x, y) = \frac{d!}{(d-1)!}\mathbf{B}^{d-1}(b(x, y))P^{d,d-1}(a_y) \cdot c^t + \eta_y(x, y), \tag{3-22}$$

with $d \geq 1$ the polynomial degree of the spline, and with a_x and a_y the directional coordinates of respectively u_x and u_y with respect to triangle t. The matrix $P^{d,d-1}(u)$ is the so-called De Casteljau matrix [42] and $\eta_x(x, y)$ and $\eta_y(x, y)$ contains the measurement noise as well as modeling errors.

The computation of the spline coefficients can be written as a linear least square problem with constraints, such that the variance of the noise terms $\eta_x(x, y)$ and $\eta_y(x, y)$ is minimized. However, the continuity constraints (3-20) need an additional constraint for producing a well-conditioned parameter estimation problem. This constraint is called the anchor constraint,

which predefines the value of the unknown constant of integration which arises when solving the first order partial differential equation of (3-4) and (3-5). If $a = \begin{bmatrix} 1 & 0 & \cdots & 0 \end{bmatrix}$ is the anchor vector, then the anchor constraint is given by

$$ac = 0. \tag{3-23}$$

The SABRE problem for a total of K slope measurements on a complete triangulation consisting of J triangle follows from (3-21) and (3-22):

$$\sigma = d\mathbf{B}^{d-1} P_u^{d,d-1} c + n, \tag{3-24}$$

$$0 = Hc, \tag{3-25}$$

where $\sigma \in \mathbb{R}^{K \times 1}$ denotes the vector of measured wavefront slopes. The residual term n contains both the sensor noise as well as the modeling errors. The matrix H in (3-25) is the constraint matrix, defined as follows:

$$H := \begin{bmatrix} A^T & a^T \end{bmatrix}^T. \tag{3-26}$$

In [6] a Linear Least Squares (LLS) estimator is presented for the B-coefficients. First of all, the constraint equation (3-25) needs to be eliminated. This can be done by projecting the system on the nullspace of the constraint matrix H defined in (3-26), i.e. $\text{null}\,(H)$. Now the problem can be formulated as an unconstrained linear regression problem:

$$\sigma = Dc + n, \tag{3-27}$$

with D given by

$$D = d\mathbf{B}^{d-1} P_u^{d,d-1} \bar{H}. \tag{3-28}$$

Here $\bar{H}$ is a basis of $\text{null}\,(H)$. The cost function is then given by

$$J(c) = \left(\sigma^T - Dc\right)^T \left(\sigma^T - Dc\right). \tag{3-29}$$

The LLS estimator for the B-coefficient of the SABRE model which minimizes the cost function (3-29), is:

$$\begin{aligned} \hat{c}_{LLS} &= \bar{H}(D^T D)^{-1} D^T \sigma \\ &= Q\sigma. \end{aligned} \tag{3-30}$$

Matrix $Q = \bar{H}(D^T D)^{-1} D^T$ is called the SABRE reconstruction matrix which is computed only once for a given geometry. Using (3-30), the resulting LLS SABRE model is

$$\phi(x) = \mathbf{B}^d \hat{c}_{LLS}. \tag{3-31}$$

3-3-3 SABRE with intensity measurements

Polo et al. proposed a method that uses the complete intensity measurements from a Hartmann sensor and not only the measured slopes [38]. Unfortunately, this method is not suitable for real-time application, because a non-convex function has to be minimized. However, Silva et al. used this work to derive a method that is also useful for real-time applications [7]. The

difference between a Hartmann sensor and a Shack-Hartmann (SH) sensor is that a Hartmann sensor consists of an array of apertures, while a SH sensor consists of an array of lenses. In this subsection, it will be shown how the method proposed by Silva et al. can also be used for a SH sensor.

Consider $F(x_i, y_j)$ to be the measured intensities of each pixel (i, j) at the detection plane and let $I(x_i, y_j, c)$ be the intensity given by the model of the particular sensor and the phase given by (3-17) with phase coefficients equal to c. Then the cost function for determining the coefficients can be defined as follows:

$$J(c) := \sum_{i,j} \left(F(x_i, y_i) - I(x_i, y_i, c)\right)^2 . \tag{3-32}$$

The cost function (3-32) is rewritten using two vectors $f \in \mathbb{R}^{M\times 1}$ and $i(c) \in \mathbb{R}^{M\times 1}$ which contain the data of $F(x_i, y_i)$ and $I(x_i, y_i, c)$ respectively for a total of M pixels. Each element m of these vectors has a direct mapping to a point (x_i, y_i) in the Cartesian plane. Hence, (3-32) can be written as follows:

$$J(c) = \|f - i(c)\|_2^2 = \sum_{m=1}^{M} \left(F(m) - I(m, c)\right)^2 . \tag{3-33}$$

As (3-32) and (3-33) are highly non-linear with respect to c, therefore it is useful to linearize $i(c)$ with respect to c, such that the cost function depends quadratically on c. In general the linearization could be around any vector $\tilde{c}$, but in this chapter it is assumed that $\tilde{c} = 0$, because it is assumed that the aberrations are small. After linearization the cost function (3-33) becomes:

$$J_{lin}(c) = \|f - (c_0 + C_1 c)\|_2^2 . \tag{3-34}$$

The vector c_0 can be obtained with the model of $i(c)$ with $c = 0$, i.e.

$$c_0 = [i(c)]_{c=0} . \tag{3-35}$$

The matrix $C_1 \in \mathbb{R}^{M\times K}$ represent the Jacobian matrix, i.e.

$$C_1 = \nabla_c i(c). \tag{3-36}$$

If the propagated beams from one sub-aperture have no effect on the subimage corresponding to another sub-aperture, then C_1 will be block-diagonal. In this chapter it is assumed that the effect of the propagated beams from one sub-aperture has a neglectable influence on other sub-aperture, because the aberrations are assumed to be small.

Minimizing this cost function will give an LLS estimator of the optimization coefficients c. Because SABRE is used, the continuity constraints has be added to the minimization problem. Hence, the vector c can be computed by solving the following minimization problem:

$$\begin{aligned} c = &\arg\min_c J_{lin}(c). \\ &\text{s.t.} \quad Hc = 0. \end{aligned}$$

The solution can be found in a similar manner as the solution of the problem (3-24)-(3-25):

$$\begin{aligned} \hat{c}_{LLS} &= \bar{H}\left(\left(C_1\bar{H}\right)^T\left(C_1\bar{H}\right)\right)^{-1}\left(C_1\bar{H}\right)^T(f - C_0) \\ &= Q\,(f - c_0)\,. \end{aligned} \tag{3-37}$$

With a simulation is shown that this linear method provides an improvement of approximately one order of magnitude in terms of RMS error regarding the classical methods for aberrations smaller than λ [7]. Another advantage of this method is that this method has the potential to be solved in a distributive manner.

For a SH sensor the measured intensity for a single sub-aperture can be computed using (3-3). From this formula it can be seen that the same intensity pattern can be obtained for different phases. Assume for example that the phase equals $-\varphi(-r)$ and a symmetric real pupil is used (i.e. $P(r) = P(-r) = \bar{P}(-r)$), then the intensity becomes:

$$\begin{aligned} I(\alpha) &= \frac{1}{\Pi}|\mathcal{F}\left[e^{-i\phi(-u)}P(u)\right]|^2 = \frac{1}{\Pi}|\mathcal{F}\left[e^{-i\phi(-u)}\overline{P}(-u)\right]|^2 = \frac{1}{\Pi}|\mathcal{F}\left[\overline{\psi}(-u)\overline{P}(-u)\right]|^2 \\ &= \frac{1}{\Pi}|\overline{\mathcal{F}\left[\psi(u)P(u)\right]}|^2 = \frac{1}{\Pi}|\mathcal{F}\left[\psi(u)P(u)\right]|^2. \end{aligned} \tag{3-38}$$

Note that here the conjugation property of the Fourier transform is used. As can be seen, (3-3) and (3-38) are equal. This problem is referred to the non-uniqueness problem.

Let $\phi_{k,i}(x,y)$ represent a possible mode of the reconstructed phase for the i-th sub-aperture and let (x,y) be the spatial coordinates with $(x,y) = (0,0)$ in the center of this sub-aperture. Suppose that this mode is symmetric within this sub-aperture, i.e. $\phi_{k,i}(x,y) = \phi_{k,i}(-x,-y)$. This would mean that this mode in not observable after linearization, because the measured intensities resulting from a phase equal to $\phi_{k,i}(x,y)$ give the same intensities as from a phase equal to $-\phi_{k,i}(-x,-y) = -\phi_{k,i}(x,y)$.

The aforementioned problem can be solved by using an additional image with the same conditions but with an additional known aberration. In this thesis use is made of two types of known aberrations, shown in figure 3-1. The first solution is a defocus before the light enters the WFS (figure 3-1a). This type of defocus will be called type I defocus. Another option is to place the photon sensor (i.e. the CCD) at another distance compared to the focus distance of the lenses, i.e. each sub-aperture is subject to a defocus. That would result in an aberration as shown in figure 3-1b and it is called type II defocus.

The computation of the SABRE coefficients with more images is almost equal to the computation of the SABRE coefficients as described in the previous subsection. Let K be the number of images and M the amount of pixels of one image. Equation (3-33) can still be used, but now $f \in \mathbb{R}^{KM\times 1}$ and $i(c) \in \mathbb{R}^{LK\times 1}$ are given by

$$\begin{aligned} f &= \begin{bmatrix} f_1^T & f_2^T & \dots f_K^T \end{bmatrix}^T, \\ i(c) &= \begin{bmatrix} i_1^T(c) & i_2^T(c) & \dots & i_K^T(c) \end{bmatrix}^T, \end{aligned}$$

with $f_i \in \mathbb{R}^{M\times 1}$ and $i_i \in \mathbb{R}^{M\times 1}$. The vector c_0 and the matrix C_1 are defined in equation (3-35) and (3-36) respectively.

3-4 Experiments with Yao

In this section, we compare the performance of gradient based SABRE and the performance of intensity based SABRE with simulations performed with Yao. First, the experiment is

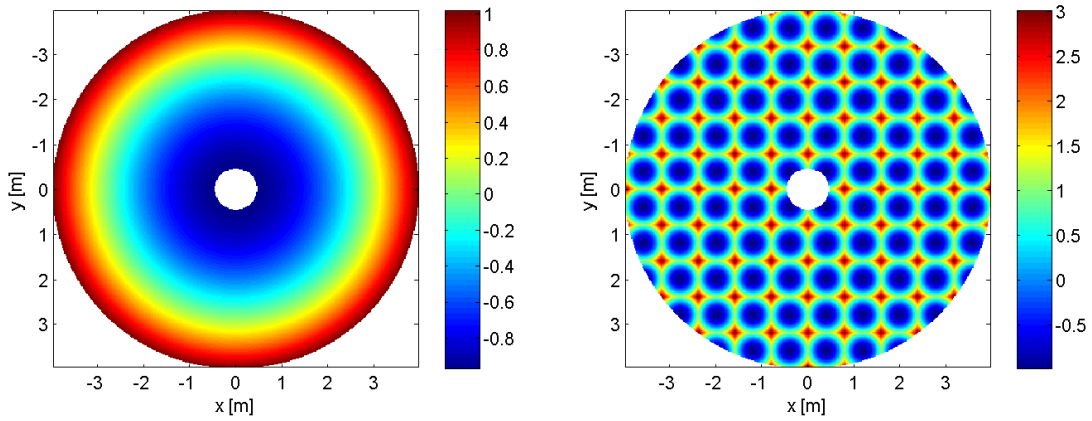

(a) Type I defocus **(b)** Type II defocus

Figure 3-1: Images of the additional known aberrations. Left: defocus for the whole image. Right: the focal plane is at a further distance than the focus distance of the lenses, so here each sub-aperture (it is a 10×10 array) has a defocus aberration. 97The aberrations are in rad.

described. Second, an example of an experiment with a fixed configuration is provided in order to concretize how the experiments are performed. Third, the influence of the different parameters is examined.

3-4-1 Description of experiments

Yorick is used to run the simulations. Yorick is an interpreted programming language for scientific simulations or calculations, postprocessing or steering large simulation codes [43]. To simulate the AO system, Yao is used [44]. Yao is an AO simulation software package which runs in Yorick. Both Yorick and Yao are open-source. Yao is used to simulate a telescope, the wavefront aberrations and the Wavefront Sensor (WFS).

Two different methods of SABRE will be considered: the gradient based SABRE and the intensity based SABRE, (see subsections 3-3-2 and 3-3-3 respectively). As part of the thesis, these methods and many other aspects of SABRE is programmed in a library of yorick. See appendix A for more details.

In these experiments a telescope with a outer diameter of $7.9m$ is considered. The inner diameter equals $0.89m$. The Kolmogorov model is used for the spectral power of the wavefront and it assumes that the light beam travels through a homogeneous turbulent medium [17]. The fried parameter r_0 defines the strength of the aberrations. With lower values of r_0 the spectral power of the wavefront increases and thus the strength of the aberrations increases as well. Typical values of the Fried parameter r_0 in the visible range from less than $5cm$ in strong turbulence during daytime to over $40cm$ at good sites at night [45]. The Fried parameter is varied during the experiments.

The atmosphere is modeled by four phase screens, moving at a speed of respectively 11, 20, 29 and $35m/s$ in the same direction. The altitudes of these layers are 0, 400, 6000 and $9000m$. The zenith angle is zero. The sample time will be $2ms$.

A SH sensor is used as sensor. The number of sub-apertures varies between 5-by-5, 6-by-6, 8-by-8, 10-by-10, 12-by-12 and 15-by-15 grids. Per sub-aperture there are 25×25 pixels. The wavelength of the measured light equals $0.65\mu m$. The SH WFS has field stops, which makes sure that light that enters one sub-apertures does not propagate into another sub-aperture. Note that therefore C_1 from (3-36) is a block-diagonal matrix.

The SH WFS can modeled with or without noise. When the SH WFS is modeled with noise, then there are two types of noise:

1. Photon noise: This is random noise with a Poisson distribution.
2. Read out noise: This is random noise with a Gaussian distribution with a mean of zero and a standard deviation of 3.5 electrons per pixel.

For the WFR only first order B-splines are used, i.e. $d = 1$. Furthermore, $r = 0$, which means that the reconstructed phase will be continuous.

A type I and type II triangulation will be used. With type I triangulation two triangles are defined within one square and with type II triangulation four triangles are used. The triangulation also depend on the method which is used, so for gradient based SABRE [6] the triangulation differ a bit compared to the triangulation with intensity based SABRE [7]. In figure 3-2, the type I and type II triangulations are shown for both gradient based SABRE and intensity based SABRE.

The SH sensor consists of a square array of sub-apertures. Because the telescope has a circular shape, some sub-apertures are not illuminated as much as others. If too little light reaches a sub-aperture, the measurement of that particular sub-aperture will be ignored. For example with a 6-by-6 array, the sub-apertures at the corners are ignored. This means that the phase is not reconstructed everywhere. When the reconstructed phase (ϕ) is compared with the real phase (φ), only the locations where the reconstructed phase is defined are considered.

In order to see how a certain configuration performs, the following expression is used as performance indicator:

$$P = \frac{RMS(\varphi - \phi)}{RMS(\varphi)} 100\%. \tag{3-39}$$

P is called the performance indicator. The RMS is defined as follows:

$$RMS(\varphi) = \sqrt{\frac{1}{A} \int_A \varphi^2 dA}, \tag{3-40}$$

where A is defined as the area in the pupil where the phase is reconstructed. Note that the mean of φ and ϕ is zero, i.e. $\int_A \varphi dA = 0$ and $\int_A \phi dA = 0$. In the ideal case, i.e. when $\phi = \varphi$, we have $P = 0$. The higher the values of P, the worse the performance is and with $P \geq 100\%$ the result of the WFR can be seen as useless.

The phase screens and measurement noise are a result of a stochastic process, so more measurements are used in order to get a good indication how a certain configuration performs. When an average performance is presented, the average is computed over 2000 different measurements, i.e. the average performance over 4 seconds.

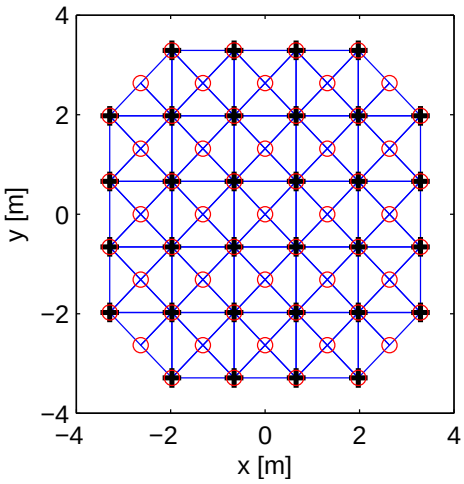

(a) Type I Triangulation for gradient based SABRE

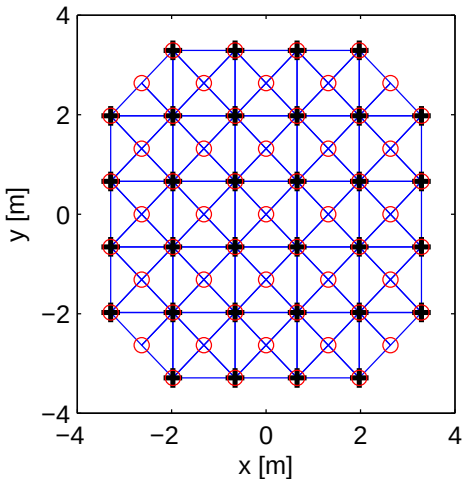

(b) Type II Triangulation for gradient based SABRE

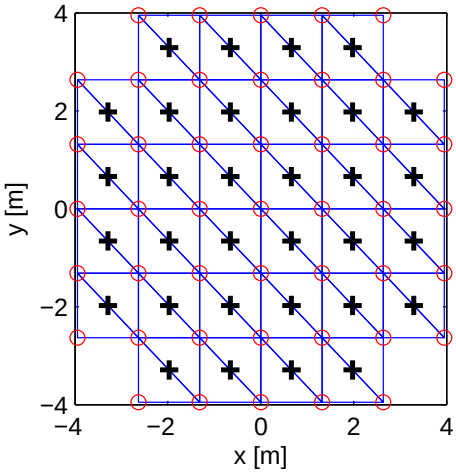

(c) Type I Triangulation for intensity based SABRE

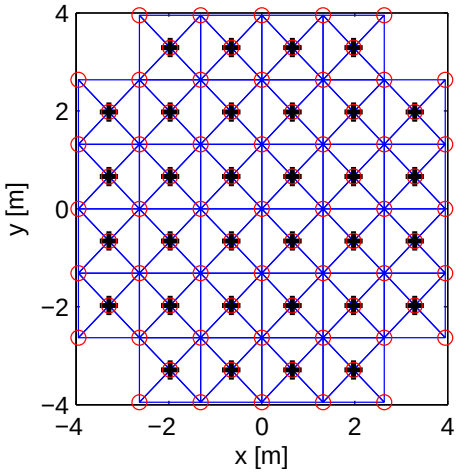

(d) Type II Triangulation for intensity based SABRE

Figure 3-2: Type I and type II triangulations for gradient based SABRE and intensity based SABRE for a SH WFS with 6×6 sub-apertures. The red circles show the vertices. The blue solid lines represent the edges of the triangles. The black crosses represent the centers of the sub-apertures.

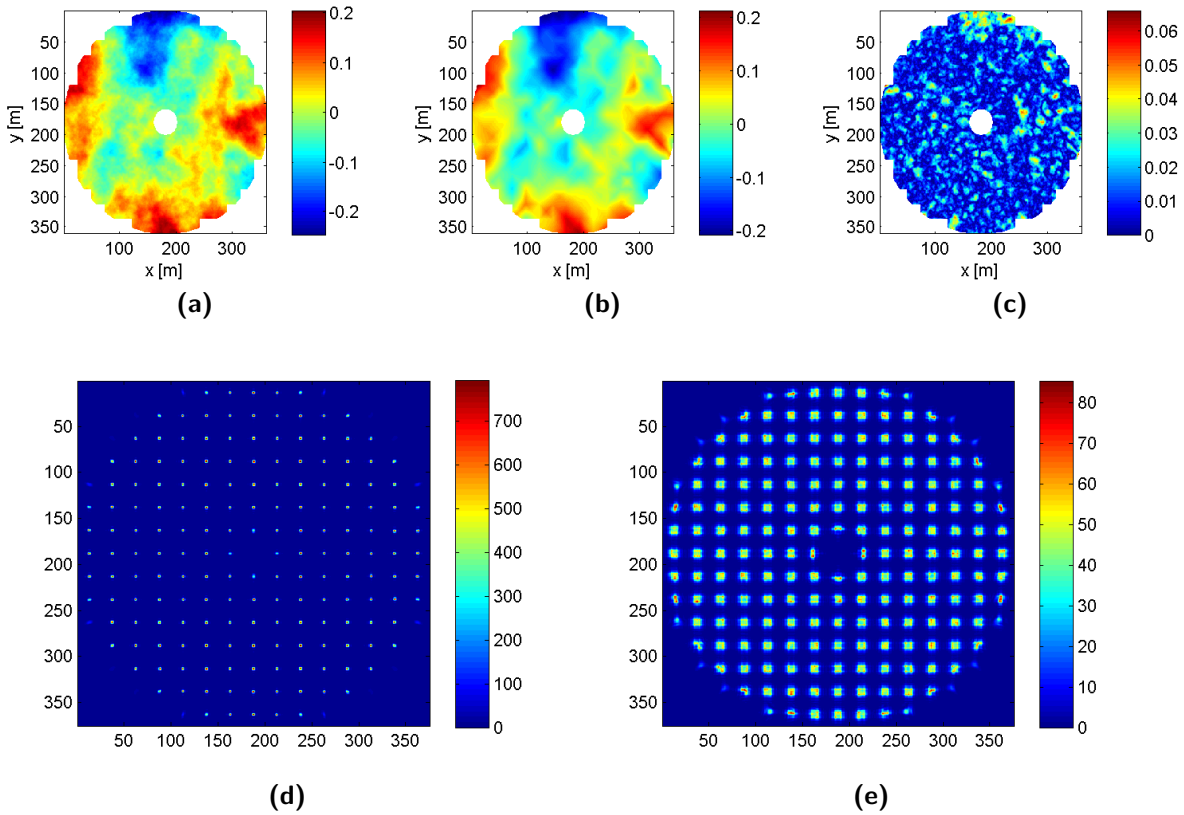

Figure 3-3: An example of a WFR with SABRE with a SH WFS with 15×15 sub-apertures and $r_0 = 2m$ with (a) the original phase, (b) the reconstruction of the phase and (c) the absolute error between the original phase and the reconstructed phase. The units of the phase are μm. The figures (d) and (e) show the image of the SH sensor where for (e) an additional defocus aberration for each sub-aperture is applied.

3-4-2 Example of one experiment

In figure 3-3, an example is shown for a WFR with a SH WFS with a 15×15 array of sub-apertures with $r_0 = 2m$. The original phase is shown in figure 3-3a. The reconstruction (see figure 3-3b) is done using the intensity based SABRE as described in section 3-3-3. In figure 3-3c, the absolute difference between the original phase of figure 3-3a and the reconstruction phase of figure 3-3b is shown. From here it can be seen that the error mainly consists of high spatial frequencies. The RMS of the aberration equals $0.0746\mu m$ and the RMS of the error equals $0.0146\mu m$, which results in $P = 19.5\%$. Figure 3-3d shows the image which is obtained by the SH WFS and figure 3-3e displays the image of the SH WFS with the additional defocus aberration.

In figure 3-4, the performance (3-39) is plotted over time. As can be seen the performance varies much from time to time. The intensity method performs better than the gradient method: the average performance of the intensity method is 13.5 %, which is better than the average performance of the gradient method (i.e. 16.5 %). This can be explained by the fact

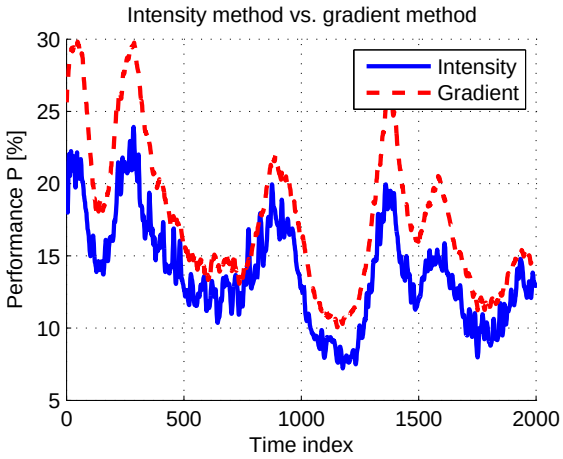

Figure 3-4: Performance (3-39) changing over time for experiment with the Fried parameter equal to $r_0 = 2m$ and a noiseless SH WFS with 15×15 sub-apertures.

that with the intensities method more information is used. Instead of only using the slopes, which are two measurements per sub-aperture, now 25×25 measurements are used. However, this is not the case for different Fried parameters, which is discussed in the next subsection.

3-4-3 Effect of defocus on intensity based SABRE

In figure 3-5, the performance of the intensity based SABRE is plotted for SH sensors with different numbers of sub-apertures and varying amount of defocus. The test is done for SH sensors with 6×6, 8×8 and 10×10 sub-apertures. In all cases, a type II triangulation is used.

As can be seen in figure 3-5a when the amount of defocus type I is too large, the performance is bad. This can be explained from the fact that the gradient of the defocus aberration will be too large, especially for the sub-apertures near the outside radius. Therefore the focus spot - and thus all information - of the sub-apertures will be outside of the sub-apertures.

From figure 3-5a it can be seen that the influence of the amount of defocus is quite different for different sensors. The optimal defocus factor for the 6×6 SH WFS is $9.4 rad$. When this amount of defocus is applied for the 8×8 and 10×10 SH WFS the performance is already worse compared to the optimal amount of defocus for these SH sensors. This makes it difficult to draw a general conclusion for the optimal amount of defocus with this method.

The influence of the amount of defocus for the second method depends less on the SH WFS geometry (see figure 3-5b) and the optimal amount of defocus type II results in a better performance compared to defocus type I. Therefore, in the remaining experiments, this method will be used. The defocus factor will be equal to $0.285\ rad$, which is the optimal point for the 6×6 SH WFS. Although this is not optimal for other SH WFS geometries, it is very close to the optimal amount of defocus.

With method II, the known aberration - which is the defocus for each sub-aperture - is equal for each sub-aperture. With method I the known aberrations are different for each sub-aperture. For example, the sub-apertures near the center do almost not have an aberration.

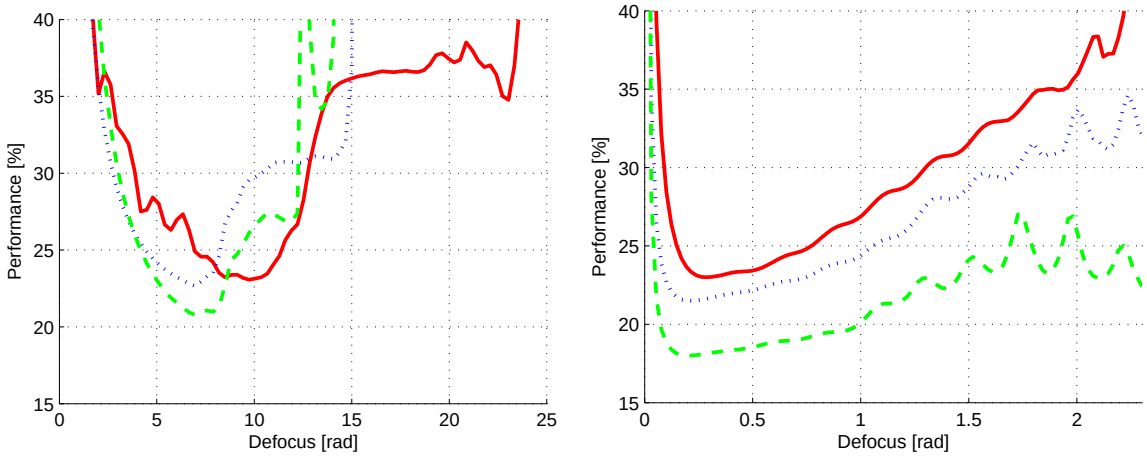

(a) Performance defocus type I **(b)** Performance defocus type II

Figure 3-5: Performance of the intensity based SABRE for a different amount of sub-apertures. The red solid line, the blue dotted line and the green dashed line represent the performance with a SH WFS with a 6×6, 8×8 and 10×10 array respectively. The x-axis shows the factor by which the unit defocus (see figure 3-1) is multiplied and the y-axis shows the performance as defined in (3-39).

Table 3-1: Optimal amount of defocus for type I defocus and type II defocus for SH sensors with different amount of sub-apertures and the corresponding performance.

	Type I defocus		Type II defocus	
Number of sub-apertures	Optimal defocus $[rad]$	Performance $[\%]$	Optimal defocus $[rad]$	Performance $[\%]$
6×6	9.4	23.1	0.29	23.0
8×8	7.0	22.7	0.22	21.5
10×10	7.0	20.8	0.19	18.0

Therefore the estimation of the coefficients is not really improved for the sub-aperture near the center. This effect will be larger when more sub-apertures are used. The results - summarized in table 3-1 - confirm this.

3-4-4 Triangulation

In this subsection, the performance of the type I triangulation and type II triangulation are compared. In table 3-2, the average performance is shown for the two different types of triangulation. The comparison is done for both gradient based SABRE and intensity based SABRE, both with and without noise. This experiment is done with a SH WFS with 6×6 sub-apertures.

With type II triangulation more simplices are used. Therefore the range of shapes which can be modeled is larger. This implies that the WFR could be more accurate. As can be seen

Table 3-2: Average performance of SABRE in combination with a SH WFS with 6×6 sub-apertures for type I and type II triangulation.

		Average performance [%]	
SABRE method	Noise	Type I triangulation	Type II triangulation
Gradient	No	42.46	36.18
Gradient	Yes	43.01	36.82
Intensity	No	29.05	24.37
Intensity	Yes	29.07	24.39

in table 3-2 the performance with type II triangulation is better than the performance with type I triangulation in the noiseless case.

The downside of using more simplices is that also more coefficients need to be estimated with the same amount of data, which can result in a higher sensitive reconstruction with respect to sensor noise. With gradient based SABRE each triangle has six and four measurements with type I and type II triangulations respectively. Although the difference is not significant, the performance difference between the reconstruction with sensor noise and without sensor noise is higher when type II triangulation is used (0.64%) compared to the type I triangulation (0.55%). Despite this result, the performance is still better when type II triangulation is used. With intensity based SABRE, the difference between the reconstructions with sensor noise and without sensor noise is neglectable (0.02%).

From the aforementioned results it can be concluded that type II triangulation gives better results than type I triangulation. Therefore for the next experiments a type II triangulation will be used.

3-4-5 Effect of Fried parameter r_0 and the amount of sub-apertures

If the Fried parameter decreases, then $RMS(\varphi)$ increases an the the linearization of equation (3-34) is not valid anymore, because the linearization is only valid for small aberrations. This results in worse performance for lower values of r_0, which can also be seen in figure 3-6. In figure 3-6, the performance is plotted with respect to the Fried parameter r_0. The experiments are done for a SH WFS with 5×5, 6×6, 8×8, 10×10, 12×12 and 15×15 sub-apertures. The results from 3-6 are based on noiseless measurements.

As can be seen in figure 3-6a the performance of the gradient method does not differ significantly for different Fried parameter, with the exception of low values of r_0. Only at the lowest value of r_0, i.e. $r_0 = 0.05m$, the performance is significantly worse than at other values of r_0. This can be explained from the fact that the gradients starts to get too high, such that the focus spot of one sub-aperture is partly outside the area of the corresponding sub-aperture. From figure 3-6a, it can also be observed that the performance is better when more sub-apertures are used. This can be explained from the fact that also the degree of freedom of the reconstructed aberration is higher when more sub-apertures are used. The reconstruction models the aberrations such that within each simplex the aberration is a tilt, since the polynomial degree d is equal to one. Because of this assumptions there will be an error and

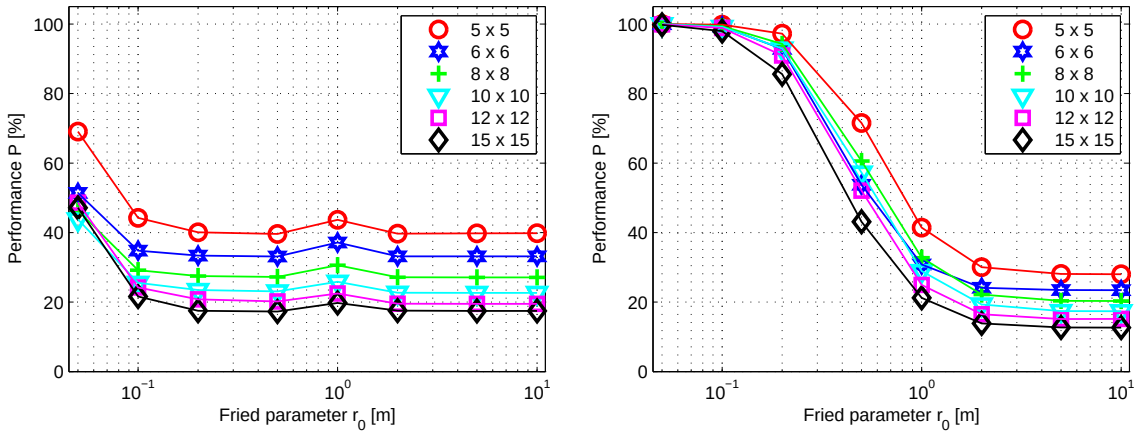

(a) Gradient based SABRE **(b)** Intensity based SABRE

Figure 3-6: The performance versus the Fried parameter r_0 for (a) gradient based SABRE and (b) intensity based SABRE with a SH WFS without measurement noise. The legend indicate the number of sub-apertures for the corresponding SH WFS.

the error will be smaller when the simplices are smaller. Hence, with more sub-apertures the error will decrease.

If intensity based SABRE is used, then the Fried parameter influences the performance very much (see figure 3-6b). The lower the Fried parameter, the lower the aberrations, the more the linearization becomes invalid. The effect of the amount of sub-apertures is the same as with gradient based SABRE: the more sub-apertures, the better the result.

In figure 3-7, the effect of the amount of sub-apertures is shown in a different manner. Here the x-axis represent the number of sub-apertures on one side of the SH WFS. When the amount of turbulence is low (i.e. $r_0 \geq 2m$), then the intensity method performs better than the gradient method. However, with for example $r_0 = 0.1m$, the phase estimates of the intensity method are completely wrong, as the linearization is not valid anymore.

3-4-6 Effect of noise

Figure 3-7 shows that more sub-apertures result in better performance. However, this is when there is no sensor noise modeled. With sensor noise the results are different, as can be seen in figure 3-8. Especially the gradient method performs worse when the number of sub-apertures is increased. With more sub-apertures, each sub-aperture will be less illuminated. Hence, the signal-to-noise ratio will decrease. Because the centroid algorithm, which is used to compute the slopes, is sensitive to noise [46], the reconstructed phase becomes worse. The results for the intensity method does not change significantly, so it can be concluded that the intensity method is less sensitive to noise compared to the gradient method.

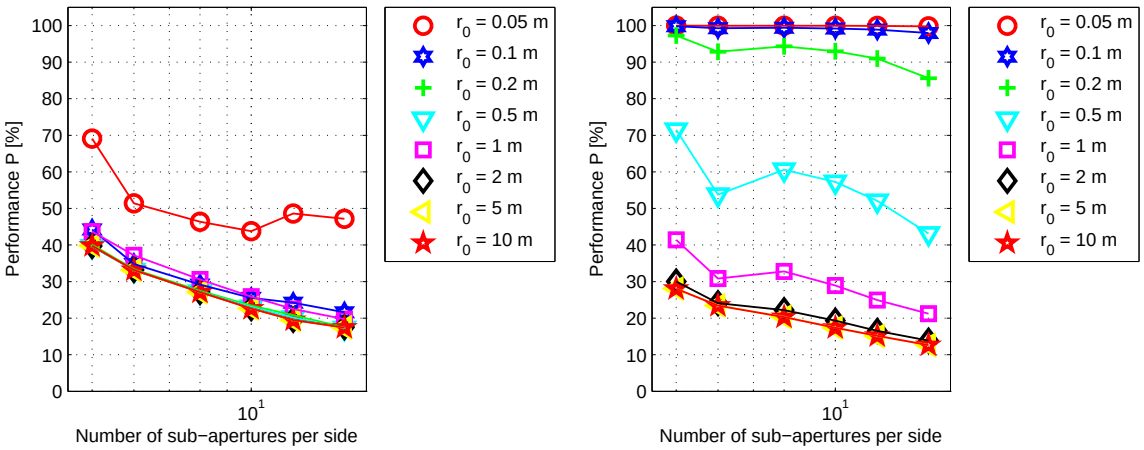

(a) Gradient based SABRE **(b)** Intensity based SABRE

Figure 3-7: The performance versus the number of sub-apertures per side for (a) gradient based SABRE and (b) intensity based SABRE with a SH WFS without measurement noise. The legend indicate the Fried parameter r_0 for the corresponding experiment.

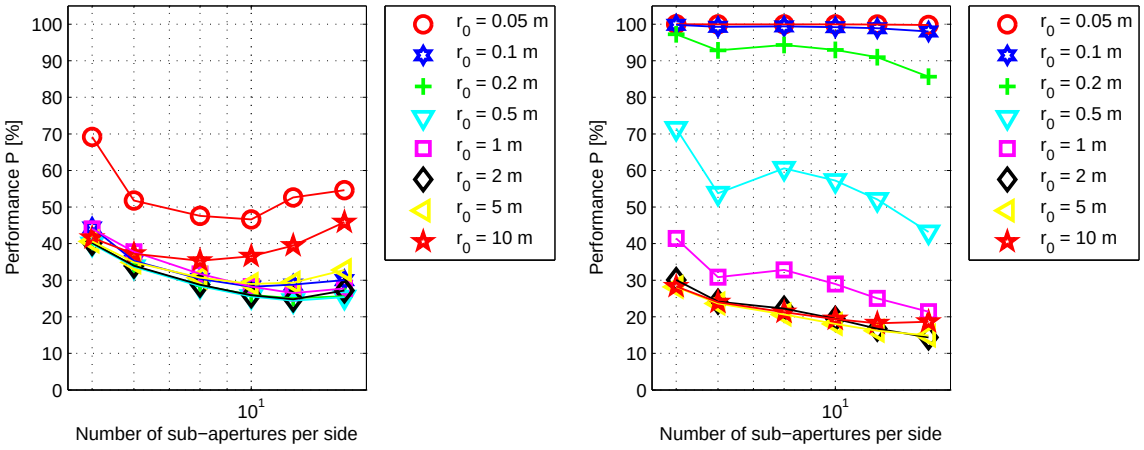

(a) Gradient based SABRE **(b)** Intensity based SABRE

Figure 3-8: The performance versus the number of sub-apertures per side for (a) gradient based SABRE and (b) intensity based SABRE with a SH WFS with measurement noise. The legend indicate the Fried parameter r_0 for the corresponding experiment

3-5 Conclusion

This chapter focuses on the modeling of the spatial dynamics of wavefront aberrations. SABRE is used for the WFR. The intensity based SABRE is adapted, such that it could be used for a SH WFS. This is achieved by adding a measurement with a SH WFS with the same blurring conditions, but with an additional known aberration.

Two methods have been discussing, namely a method that uses the whole intensity pattern measured by the CCD of the SH WFS and a method that uses the local slopes, which are computed using the centroid algorithm. Those two methods are compared in a AO simulation. Therefore, as part of this project, a SABRE library have been written. From the experiments the following could be concluded:

- The intensity based SABRE reconstructs the wavefront more accurately compared to the gradient based SABRE for small aberrations. For ground-based telescopes, the Fried parameter is smaller than $r_0 = 0.4m$. Intensity based SABRE performs better than gradient based SABRE for $r_0 > 1m$. However, this could be different when the loop is closed by using a DM, however, because then the aberrations will be smaller.
- The intensity based SABRE showed to be much more noise robust when compared with gradient SABRE.

Chapter 4

Autonomous Subspace Identification

4-1 Introduction

Subspace Identification (SID) methods are methods that identify Linear Time Invariant (LTI) state-space models from Multiple Input Multiple Output (MIMO) measurements of a dynamic system. For a detailed description we refer the reader to the literature [47, 48]. An advantage of SID methods is the fact that the key operations are all linear algebra operations so the problem of nonlinear optimization is circumvented.

In this chapter a special type of SID is treated: Autonomous Subspace Identification (ASID). This means that the only input of the system is some unknown noise. The two methods which will be shown are based on the Past Output Multivariable Output-Error State sPace (PO-MOESP) method [49] and the Predictor Based Subspace Identification (PBSID) method [50]. These SID methods are intended to be used in off-line identification.

The outline of this article is as follows. We will first start with the system description, assumptions and notation in section 4-2. In section 4-3, two ASID methods will be described. In section 4-4, the proposed algorithms are tested for identification of a fictive second order system.

4-2 System description, assumptions and notations

The to be modeled system can be described with the following state space model:

$$x(k+1) = Ax(k) + w(k), \tag{4-1}$$
$$y(k) = Cx(k) + v(k), \tag{4-2}$$

where $x(k) \in \mathbb{R}^n$, $y(k) \in \mathbb{R}^l$, $w(k) \in \mathbb{R}^n$ and $v(k) \in \mathbb{R}^l$ are the state, output, process noise and measurement noise vectors respectively and k denoted the time index. The state matrix is denoted by $A \in \mathbb{R}^{n \times n}$ and $C \in \mathbb{R}^{l \times n}$ is called the output matrix. It is assumed that $w(k)$

and $v(k)$ are zero-mean white noise sequences. The system (4-1)-(4-2) can also be written in innovation form [47]:

$$\hat{x}(k+1) = A\hat{x}(k) + Ke(k), \tag{4-3}$$
$$y(k) = C\hat{x}(k) + e(k), \tag{4-4}$$

where $e(k) \in \mathbb{R}^l$ is called the innovation with $\mathbf{E}\left[e(k)e^T(k)\right] = R$. It is assumed that R is positive definite. Matrix $K \in \mathbb{R}^{n\times l}$ is the Kalman gain. In (4-3)-(4-4), the state is denoted by $\hat{x} \in \mathbb{R}^n$, which is the predicted state of $x(k)$ such that $\mathbf{E}\left[\hat{x}(k) - x(k)\right] = 0$ and $\mathbf{E}\left[\left(\hat{x}(k) - x(k)\right)\left(\hat{x}(k) - x(k)\right)^T\right]$ is minimal. It is assumed that the system (4-3)-(4-4) is a minimal realization, i.e. the pair (A, K) is controllable and (A, C) is observable. This system (4-3)-(4-4) can also be written in the so-called predictor form:

$$\hat{x}(k+1) = \tilde{A}\hat{x}(k) + Ky(k), \tag{4-5}$$
$$y(k) = C\hat{x}(k) + e(k), \tag{4-6}$$

where $\tilde{A} = A - KC$ is asymptotically stable. It is assumed that $\tilde{A}$ is nilpotent, i.e. $A^j = 0$ for $j \geq k$ with $k \in \mathbb{N}$. It is well-known that an invertible linear transformation of the state vector does not change the behavior of a state-space system. Therefore, we can only determine the system matrices up to an unknown similarity transformation T: $T^{-1}AT$, $T^{-1}K$ and CT.

The following stacked vector contains s outputs:

$$\bar{y}_{i,s} := \begin{bmatrix} y(i) \\ y(i+1) \\ \vdots \\ y(i+s-1) \end{bmatrix} \in \mathbb{R}^{sl}. \tag{4-7}$$

The stacked vector $\bar{e}_{i,s}$ is defined in a analogue way. With N data available the block Hankel matrix can be defined:

$$Y_{i,s,N} := \begin{bmatrix} \bar{y}_{i,s} & \bar{y}_{i+1,s} & \dots & \bar{y}_{i+N-1,s} \end{bmatrix} \in \mathbb{R}^{sl\times N}. \tag{4-8}$$

In a analogue manner $E_{i,s,N}$ can be defined. The matrix that contains N states is defined as follows:

$$X_{i,N} = \begin{bmatrix} x(i) & x(i+1) & \dots & x(i+N-1) \end{bmatrix}. \tag{4-9}$$

The matrix $\hat{X}_{i,N}$ is defined in a analogue way using the predicted states $\hat{x}(k)$.

4-3 Autonomous Subspace Identification

4-3-1 Past Output Autonomous Subspace Identification

Using the definitions of (4-8) and (4-9), the system description (4-5)-(4-6) can be written as

$$\hat{X}_{s,N} = \tilde{A}^s\hat{X}_{0,N} + \tilde{\mathcal{K}}_s Y_{0,s,N}, \tag{4-10}$$
$$Y_{s,s,N} = \mathcal{O}_s\hat{X}_{s,N} + \mathcal{S}_s E_{s,s,N}, \tag{4-11}$$

where $\tilde{\mathcal{K}}_s$ and $\mathcal{O}_s$ are the extended controllability and observability matrix respectively which are given by

$$\tilde{\mathcal{K}}_s := \begin{bmatrix} \tilde{A}^{s-1}K & \tilde{A}^{s-2}K & \dots & \tilde{A}K & K \end{bmatrix} \in \mathbb{R}^{n \times sl}, \tag{4-12}$$

$$\mathcal{O}_s := \begin{bmatrix} C \\ CA \\ \vdots \\ CA^{s-1} \end{bmatrix} \in \mathbb{R}^{sl \times n}. \tag{4-13}$$

Note that $\tilde{\mathcal{O}}_s$ is defined in an analogue way with $\tilde{A}$. The Block Toeplitz matrix $\mathcal{S}_s$ is defined as follows:

$$\mathcal{S}_s := \begin{bmatrix} I & 0 & 0 & \dots & 0 \\ CK & I & 0 & \dots & 0 \\ CAK & CK & I & \dots & 0 \\ \vdots & \vdots & \ddots & \ddots & \vdots \\ CA^{s-2}K & CA^{s-3} & \dots & CK & I \end{bmatrix} \in \mathbb{R}^{sl \times sl}. \tag{4-14}$$

In order to estimate the system matrices A and C up to a similarity transformation the range of $\mathcal{O}_s$ needs to be known. In other words, we want to eliminate the term $\mathcal{S}_s E_{i,s,N}$ in (4-11). This can be done by using an instrumental variable Z_N with the following properties:

$$\lim_{N\to\infty} \frac{1}{N} E_{i,s,N} Z_N^T = 0, \tag{4-15}$$

$$\operatorname{rank}\left(\lim_{N\to\infty} \frac{1}{N} \hat{X}_{i,N} Z_N^T \right) = n. \tag{4-16}$$

This can be achieved by setting $i = s$ and using $Z_N = Y_{0,s,N}$ as the instrumental variable. This is called the Past Output ASID (PO-ASID) method, because $Y_{0,s,N}$ contains output data which is shifted to the past compared to the output data contained in $Y_{s,s,N}$. The following lemmas proof that equations (4-15) and (4-16) hold.

Lemma 1. *Given the system* (4-3)-(4-4) *with $e(k)$ a zero-mean white noise sequence. Then we have*

$$\lim_{N\to\infty} \frac{1}{N} E_{s,s,N} Y_{0,s,N}^T = 0. \tag{4-17}$$

Proof. The proof immediately follows from the fact that $e(j)$ is uncorrelated with $y(k)$ for all $j > k$. □

Lemma 2. *Given the minimal realization* (4-3)-(4-4) *where $e(k)$ is a zero-mean white noise sequence that satisfies $\mathbf{E}\left[e(k)e^T(k)\right] = R > 0$ and $\tilde{A}^j = 0$ for all $j \geq s$ and $sl \geq n$. Then we have*

$$\operatorname{rank}\left(\lim_{N\to\infty} \frac{1}{N} \hat{X}_{s,N} Y_{0,s,N}^T \right) = n. \tag{4-18}$$

Proof. When (4-10) is substituted into (4-18) the following equation is obtained:

$$\operatorname{rank}\left(\lim_{N\to\infty} \frac{1}{N} \left(\tilde{A}^s \hat{X}_{0,N} + \tilde{\mathcal{K}}_s Y_{0,s,N} \right) Y_{0,s,N}^T \right) = n.$$

Since $\tilde{A}^s = 0$ this can be simplified to:

$$\operatorname{rank}\left(\lim_{N\to\infty}\frac{1}{N}\tilde{\mathcal{K}}_s Y_{0,s,N}Y_{0,s,N}^T\right) = n.$$

It is given that (4-3)-(4-4) is a minimal realization. Hence, we have rank $\left(\tilde{\mathcal{K}}_s\right) = n$. Furthermore since we have $R > 0$ we know that

$$\operatorname{rank}\left(\lim_{N\to\infty} Y_{0,s,N}Y_{0,s,N}^T\right) = sl.$$

This completes the proof. □

Using the result of lemma 1 and 2, we have that

$$\operatorname{range}\left(Y_{s,s,N}Y_{0,s,N}^T\right) = \operatorname{range}\left(\mathcal{O}_s\right). \tag{4-19}$$

Now consider the following QR factorization:

$$\begin{bmatrix} Y_{0,s,N} \\ Y_{s,s,N} \end{bmatrix} = \begin{bmatrix} R_{11} & 0 \\ R_{21} & R_{22} \end{bmatrix}\begin{bmatrix} Q_1 \\ Q_2 \end{bmatrix}. \tag{4-20}$$

Lemma 3. *Consider the same assumptions as in lemma 1 and 2 and the QR factorization of equation* (4-20)*. Then the following holds:*

$$\operatorname{range}\left(\frac{1}{\sqrt{N}}R_{21}\right) = \operatorname{range}\left(\mathcal{O}_s\right). \tag{4-21}$$

Proof. From (4-20) we have

$$\begin{aligned} Y_{0,s,N} &= R_{11}Q_1, \\ Y_{s,s,N} &= R_{21}Q_1 + R_{22}Q_2. \end{aligned}$$

Hence, we obtain

$$Y_{s,s,N}Y_{0,s,N}^T = R_{21}Q_1Q_1^TR_{11}^T + R_{22}Q_2Q_2^TR_{11} = R_{21}R_{11}^T.$$

Because $R > 0$ we know that

$$\operatorname{rank}\left(\lim_{N\to\infty}\frac{1}{N}\begin{bmatrix} Y_{0,s,N} \\ Y_{s,s,N} \end{bmatrix}\right) = sl$$

and therefore $\lim_{N\to\infty}\frac{1}{\sqrt{N}}R_{11}$ is invertible. Then it can be seen with Sylvester's inequality that

$$\operatorname{rank}\left(\lim_{N\to\infty}\frac{1}{\sqrt{N}}R_{21}\right) = n.$$

This yields

$$\operatorname{range}\left(\lim_{N\to\infty}\frac{1}{\sqrt{N}}R_{21}\right) = \operatorname{range}\left(\mathcal{O}_s\right).$$

□

The system matrices A and C can be computed with a Singular Value Decomposition (SVD) of $\frac{1}{\sqrt{N}}R_{21}$. Therefore consider the following SVD:

$$\frac{1}{\sqrt{N}}R_{21} = \begin{bmatrix} U_n & U_\perp \end{bmatrix} \left(\begin{bmatrix} \Sigma_n & 0 \\ 0 & 0 \end{bmatrix} + \Sigma_{noise} \right) \begin{bmatrix} V_n^T \\ V_\perp^T \end{bmatrix}. \tag{4-22}$$

The first l rows of U_n equal C. The state matrix A can be computed using the matrices $\bar{U}_n$ and $\underline{U}_n$ where $\bar{U}_n$ equals U_n without the bottom l rows and $\underline{U}_n$ equals U_n without the l upper rows:

$$A = \bar{U}_n^\dagger \underline{U}_n. \tag{4-23}$$

The PO-ASID algorithm is summarized in 1.

Algorithm 1. *PO-ASID*
Input: y, n, s.
Step 1: Construct $Y_{0,s,N}$ and $Y_{s,s,N}$ using (4-8).
Step 2: Compute R_{21} using QR factorization of (4-20).
Step 3: Compute U_n using the SVD of (4-22).
Step 4: Extract C from the first l rows of U_n and compute A using (4-23).

4-3-2 Autonomous Predictor Based Subspace Identification

Predictor Based Subspace Identification (PBSID) is a well-known identification technique [50, 51, 52]. It uses the predictor system (4-5)-(4-6) to compute the so-called Markov parameters from input-output data. From that it estimates the states $\hat{x}(k)$. Finally the system matrix can be found by using a Linear Least Squares (LLS) solution, while also the innovation $e(k)$ is estimated. The method which will be presented here is called Autonomous PBSID (APBSID) as it uses the same strategy: it will first estimate the Markov parameters, then the states and finally the system matrices.

The first step is to estimate the Markov parameters, which are defined as follows:

$$\tilde{\Xi}^{(y_{k-i})} = C\tilde{A}^{i-1}K.$$

Here, p is the so-called past window. With the Markov parameters the output at time instant k can be estimated using the output data where it is assumed that $\tilde{A}^j = 0$ for all $j \geq p$:

$$\hat{y}(k|k-1) = \sum_{i=1}^{p} \tilde{\Xi}^{(y_{k-i})} y(k-i) = \tilde{\Xi}\bar{y}_{k-p,p}, \tag{4-24}$$

where $\hat{y}(k|k-1)$ denotes the estimated output of time instant k using output data from time instants $k-p$ to $k-1$ and

$$\tilde{\Xi} = \begin{bmatrix} \tilde{\Xi}^{(y_{k-p})} & \tilde{\Xi}^{(y_{k-p+1})} & \dots & \tilde{\Xi}^{(y_{k-1})} \end{bmatrix}.$$

The prediction (4-24) can be done for each time instant k from p to $p+N-1$. Hence, $\tilde{\Xi}$ can be approximated by solving the following equation:

$$Y_{p,1,N} = \tilde{\Xi} Y_{0,p,N}.$$

The solution can be found using a LLS solution:

$$\tilde{\Xi} = Y_{p,1,N} Y_{0,p,N}^{\dagger}, \tag{4-25}$$

where † denotes the pseudo inverse. The second step is to estimate the states. With the output data the states can be computed using the extended controllability matrix $\tilde{\mathcal{K}}_p$ defined in (4-12). Matrix $\tilde{\mathcal{K}}_p$ is unknown, but with $\tilde{\Xi}$ the matrix $\tilde{\mathcal{O}}_f \tilde{\mathcal{K}}_p$ can be computed and thus we can compute:

$$\tilde{\mathcal{O}}_f \hat{X}_{p,N} = W \tilde{\mathcal{O}}_f \tilde{\mathcal{K}}_p Y_{0,p,N}. \tag{4-26}$$

Here, $W \in \mathbb{R}^{lf \times lf}$ is a weight matrix, which can be identity. For a discussion on how to choose the weighting matrix we refer the reader to [50]. The future window is denoted by f. The matrix $\tilde{\mathcal{O}}_f \tilde{\mathcal{K}}_p$ can be constructed from the estimated Markov parameters:

$$\tilde{\mathcal{O}}_f \tilde{\mathcal{K}}_p = \begin{bmatrix} \tilde{\Xi}^{(y_{k-p})} & \dots & \tilde{\Xi}^{(y_{k-p+f-1})} & \dots & \tilde{\Xi}^{(y_{k-1})} \\ 0 & \dots & \tilde{\Xi}^{(y_{k-p+f-2})} & \dots & \tilde{\Xi}^{(y_{k-2})} \\ \vdots & \ddots & \vdots & \ddots & \vdots \\ 0 & \dots & \tilde{\Xi}^{(y_{k-p})} & \dots & \tilde{\Xi}^{(y_{k-f})} \end{bmatrix}. \tag{4-27}$$

With an SVD of (4-26) the states can be estimated up to a similarity transformation:

$$\hat{X}_{p,N} = \Sigma_n^{1/2} V_n^T, \tag{4-28}$$

where Σ_n and V_n can be extracted from the following SVD:

$$W \tilde{\mathcal{O}}_f \tilde{\mathcal{K}}_p Y_{0,p,N} = \begin{bmatrix} U_n & U_\perp \end{bmatrix} \begin{bmatrix} \Sigma_n & 0 \\ 0 & \Sigma_\perp \end{bmatrix} \begin{bmatrix} V_n^T \\ V_\perp^T \end{bmatrix}. \tag{4-29}$$

With the estimated states the output matrix C can be estimated using the following over-determined system of equation:

$$Y_{p,1,N} = C \hat{X}_{p,N}.$$

Using the LLS method it follows that

$$C = Y_{p,1,N} X_{p,N}^{\dagger}. \tag{4-30}$$

With the estimated output matrix C the innovation can be estimated since $y(k)$ and $\hat{x}(k)$ are known. Hence, the estimated innovation equals

$$E_{p,1,N} = Y_{p,1,N} - C \hat{X}_{p,N}. \tag{4-31}$$

Finally, the matrices A and K can be estimated using equation (4-3). Equation (4-3) can be expanded using the time instants p to $p + N - 2$ which gives

$$X_{p+1,N-1} = \begin{bmatrix} A & K \end{bmatrix} \begin{bmatrix} X_{p,N-1} \\ E_{p,1,N-1} \end{bmatrix}.$$

Now, A and K can be estimated using the LLS method:

$$\begin{bmatrix} A & K \end{bmatrix} = X_{p+1,N-1} \begin{bmatrix} X_{p,N-1} \\ E_{p,1,N-1} \end{bmatrix}^{\dagger}. \tag{4-32}$$

The APBSID method is summarized in algorithm 2.

Algorithm 2. *APBSID*
Input: y, p, f, W with $p \geq f$.
Step 1: Construct from the output data the matrices $Y_{p,1,N}$ and $Y_{0,p,N}$ using (4-8)*, such that the Markov parameters $\tilde{\Xi}$ can be estimated using* (4-25)*.*
Step 2: Construct $\tilde{\mathcal{O}}_f\tilde{\mathcal{K}}_p$ from $\tilde{\Xi}$ using (4-27)*. With the SVD of* (4-29) *the estimated states $\hat{X}_{p,N}$ can be computed according to* (4-28)*.*
Step 3: Compute C, $E_{p,1,N}$, $\begin{bmatrix} A & K \end{bmatrix}$ using equations (4-30)*,* (4-31) *and* (4-32) *respectively.*

4-4 Preliminary Simulation

Two different ASID methods are proposed, namely the PO-ASID method and the APBSID method. It has been shown that under mild conditions these methods give unbiased results. In this section, this will be confirmed with a fictive second order system. Also it will be explained how the parameters of these two methods can be tuned.

4-4-1 Description

The simulation is performed with a system described in (4-3)-(4-4) with the following system matrices:

$$A = \begin{bmatrix} -1.6 & -0.89 \\ 1 & 0 \end{bmatrix}, K = \begin{bmatrix} -0.6 \\ 0.75 \end{bmatrix}, C = \begin{bmatrix} 1 & 1 \end{bmatrix}. \tag{4-33}$$

The poles of the system are $-0.8 \pm 0.5i$. The eigenvalues of $\tilde{A} = A - KC$ are $-0.875 \pm 0.238i$. The innovation $e(k)$ is a zero-mean white noise sequence with $\mathbf{E}\left[e(j)e(k)\right] = \delta(k-j)$, where $\delta(\cdot)$ denotes the dirac function.

4-4-2 Results ASID

With the PO-ASID method the variable s needs to be chosen. With PO-ASID it is assumed that $\tilde{A}^j = 0$ for $j \geq s$, which means that an error is introduced, because $\tilde{A}$ is not nilpotent. The smaller s is, the higher the error. However, choosing s too large will result in an ill-conditioned problem for finding the extended observability matrix. This is because the innovation $e(k)$ has to be persistently exciting. The size of $\mathcal{O}_s$ increases and thus more parameters needs to be estimated. Hence, the variance of the estimated extended observability matrix will increase as well. Note that larger values of s will also increase the computational time. To see these effects consider figure 4-1a. In figure 4-1a, the PO-ASID method is tested for different values of s. For each value of s the PO-ASID is performed 100 times. For each experiment 1000 datapoints are used. The lowest RMS is achieved for $s = 15$. Hence, $s = 15$ will be used in the remaining part of this section.

With APBSID two variables need to be chosen: the past window size p and the future window size f with $p \geq f$. The effect of p is similar to the effect of s with the PO-ASID method. Choosing p too small will lead to a truncation error which is equal to the sum of the remaining tail of Markov parameters [51]. Too large values of p will lead to high variance of the estimated Markov parameters. The effect of the future window size f is harder to describe because it

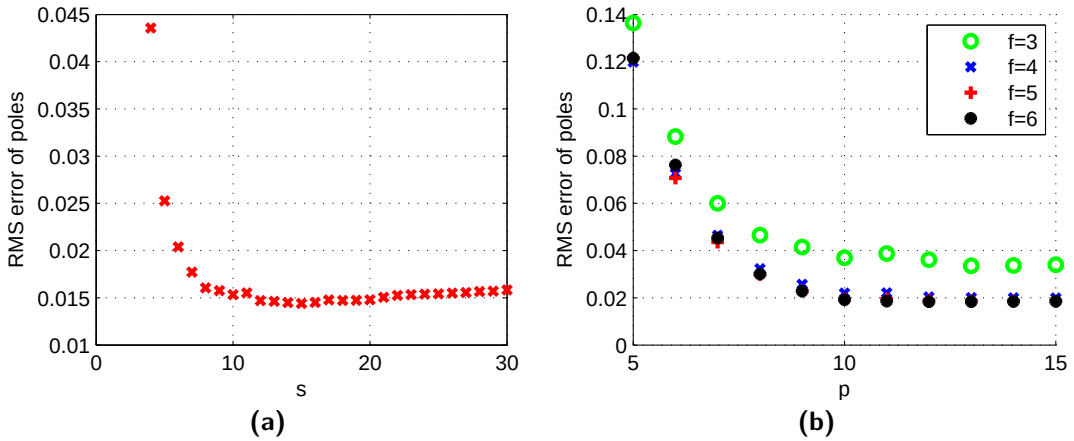

Figure 4-1: (a) The performance of the PO-ASID method for different values of s. (b) The performance of the APBSID method for different values of p and f. The performance is measured as a RMS of the distance between the real poles and the estimated poles of the system.

heavily depends on the system properties and the noise spectrum [53]. The effect of p and f for this particular experiment is shown in figure 4-1b. For the remaining part of this subsection, $p = 12$ and $f = 5$ will be used. Further increasing f and/or p does not improve the result.

In figure 4-2, one eigenvalue of the A matrix defined in (4-33) is shown, together with a pole of the estimated A matrices. The pole of the A matrix defined in (4-33) is marked by the big blue cross. The green circles and red triangles represent the poles of the estimated A matrix using the PO-ASID method and APBSID method respectively. The mean absolute error of the PO-ASID is $0.126 \cdot 10^{-3}$ which is slightly less then $0.146 \cdot 10^{-3}$, the mean absolute error of the APBSID method. Based on this result it can be concluded that the PO-ASID method performs slightly better. Note that both methods give unbiased results, i.e. when an infinite amount of experiments should be done, then the mean absolute error will approach zero.

With the APBSID method the matrix K is estimated as well as shown in figure 4-3. Here, an eigenvalue of $A - KC$ is denoted by the big blue cross. The red triangles are eigenvalues of the estimated $A - KC$ matrix. In this figure the mean absolute error is $0.120 \cdot 10^{-3}$ and the standard deviation equals $0.834 \cdot 10^{-3}$. If more experiments are used the mean absolute error will approach zero, so this result is also unbiased.

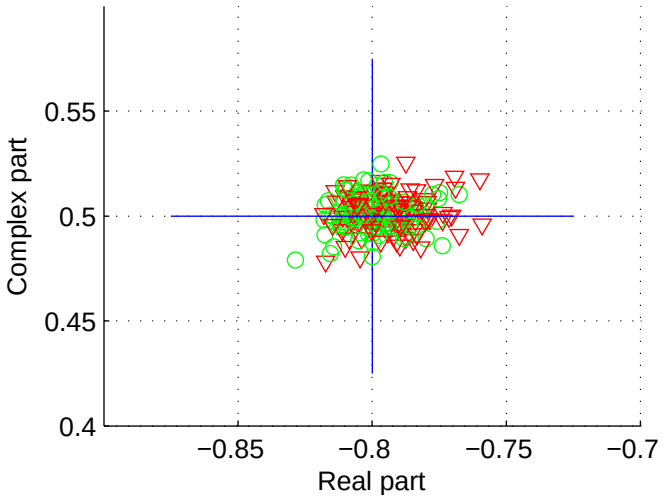

Figure 4-2: Eigenvalues of the estimated A matrices with PO-ASID (green circles) and APBSID (red triangles) next to the actual pole (big blue cross). The estimated poles are unbiased.

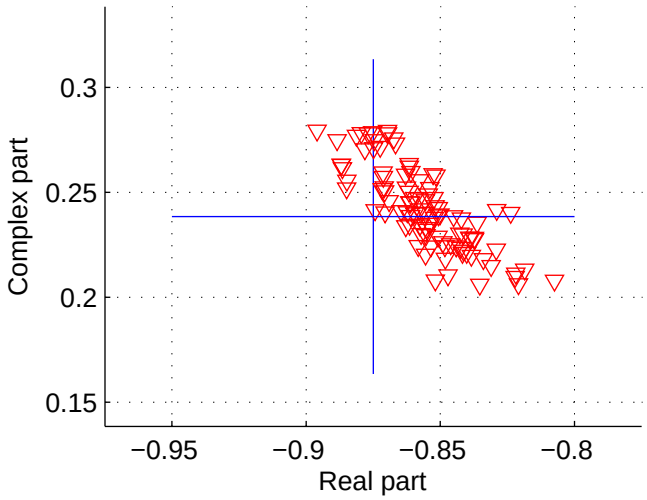

Figure 4-3: The eigenvalue of the (estimated) matrix $\tilde{A} = A - KC$ with APBSID (red triangles) next to the actual eigenvalue (big blue cross).

Chapter 5

Filtering of SABRE

In the introduction of this thesis the importance of the Wavefront Reconstruction (WFR) was discussed. The goal of the WFR is to reconstruct the phase aberration $\varphi(k)$ at time instant k with the data $s(k)$ from the Wavefront Sensor (WFS). The reconstructed wavefront is denoted with $\phi(k)$ (see also figure 2-3). This reconstructed wavefront can be used to correct for the aberrations. However, the reconstructed aberration is delayed, e.g. due to the read out and computational time in the WFS and WFR process. Therefore it would be an advantage if a good prediction is available of $\varphi(k+1)$, such that the temporal dynamics are taken into account.

This chapter is organized as follows. In section 5-1, the problem is described in more detail and it is shown why a Constrained Kalman Filter (CKF) is in our case preferable to a KF. In section 5-2, the CKF is introduced. Experiments are used to show how the different filters perform. The experiments and the results can be found in section 5-3. This section will end with some conclusions in 5-4.

5-1 Problem description

In this chapter the goal is to find a good prediction of $\varphi(k+1)$ with estimates up to time instant k. This prediction is denoted by $\phi(k+1|k)$, where the index $k+1|k$ refers to the fact that we want to predict the phase of time instant $k+1$ with data up to time instant k. The error between the estimated wavefront and the real wavefront will be called the residual wavefront.

In section 2-3, it has been shown that the objective of AO is to minimize the variance of the residual wavefront. Therefore the objective is to compute $\phi(k+1|k)$ such that the variance of the difference between $\phi(k+1|k)$ and $\varphi(k+1)$ is minimized. A Kalman Filter (KF) can be used [13]. More specifically, a KF minimizes

$$\mathbf{E}\left[(\varphi(k+1) - \phi(k+1|k))^2\right], \tag{5-1}$$

while

$$\mathbf{E}\left[\varphi(k+1) - \phi(k+1|k)\right] = 0. \tag{5-2}$$

In chapter 3, it is shown that Spline based ABerration REconstruction (SABRE) can be used for the WFR. SABRE computes a vector of spline coefficients $c(k) \in \mathbb{R}^{n_c}$ at each time instant k, based on the measurements (gradients or intensities). Note that $n_c = J\hat{d}$ where J denotes the number of simplices and $\hat{d}$ denotes the number of coefficients for each simplex. The reconstructed phase can be computed with the matrix-vector-multiplication given in equation (3-17). The next step is to predict the phase at time instant $k+1$ with all the estimates up to time instant k. In general, the amount of phase points is much larger than the amount of coefficients. Therefore it is from computational point of view better to estimate the coefficients instead of the phase. Hence, we want to compute $\hat{c}(k+1|k)$ where $\hat{c}(\cdot)$ means that it is an estimate of $c(\cdot)$, such that (5-1) is minimized and (5-2) is satisfied.

The vector $c(k)$, which is computed with SABRE, satisfies the constraint

$$Hc(k) = 0 \quad \forall k, \tag{5-3}$$

where $H \in \mathbb{R}^{n_h \times n_c}$ is the so-called constraint matrix. These constraints can be used to improve the Kalman Filter (KF). In general the KF will produce a prediction which does not satisfy the constraint (5-3). In order to predict an estimate which does satisfy the constraint (5-3) we use a CKF [54, 55]. In the remaining part of this chapter the tilde will be used to denote that the estimate satisfies the constraint, i.e. $\tilde{c}(k+1|k)$ denotes the prediction of $c(k+1)$ such that

$$H\tilde{c}(k+1|k) = 0. \tag{5-4}$$

The problem of this chapter can be summarized as follows: find an estimate of $c(k+1)$ such that (5-1) is minimized and (5-2) is satisfied. This will be done with a KF or with a CKF. With the CKF the continuity constraint (5-3) is taken into account.

5-2 Constrained Kalman Filtering for SABRE

The description of the CKF for SABRE is divided into the following subsections. In the first subsection the centralized CKF is presented. The distributed CKF is presented in 5-2-2. For the CKF the state projection method will be used, which is described in 5-2-3. In 5-2-4, an alternative state projection method is proposed. The state projection can be done in a distributive manner which is shortly described in 5-2-5.

5-2-1 Centralized CKF

For Kalman Filtering, a model description is required. As explained in 2-4-2 an autonomous system will be used. This autonomous system can be obtained using the methods of chapter 4. The result is a state description of the following form:

$$x(k+1) = A(k)x(k) + K(k)e(k), \tag{5-5}$$

$$c(k) = C(k)x(k) + e(k). \tag{5-6}$$

The matrices $A(k) \in \mathbb{R}^{n_x \times n_x}$, $K(k) \in \mathbb{R}^{n_x \times n_c}$ and $C(k) \in \mathbb{R}^{n_c \times n_c}$ can be estimated using Autonomous Subspace Identification (ASID) (see section 4-3) or Recursive Autonomous Subspace Identification (RASID). The output of the system is the vector of SABRE coefficients, $c(k)$. It is assumed that the innovation $e(k) \in \mathbb{R}^{n_c}$ is a zero-mean white noise sequence. As we will see, the state $x(k+1) \in \mathbb{R}^{n_x}$ can be predicted using the KF.

In order to estimate the system description (5-5)-(5-6), the past estimates of coefficients are used, e.g. $c(0), c(1), \ldots, c(k)$. This data satisfies the constraint (5-3). However, from computational point of view it is better to use the reduced data $\bar{c}(k) \in \mathbb{R}^{\bar{n}_c}$ such that

$$c(k) = \bar{H}\bar{c}(k), \tag{5-7}$$

where $\bar{H} \in \mathbb{R}^{n_c \times \bar{n}_c}$ is an orthogonal basis of the null space of H. The first advantage is that $\bar{c}(k)$ is a vector with equal or less entries than the vector $c(k)$ (i.e. $\bar{n}_c \leq n_c$). Hence, the computational effort might be less. Second, when the estimate $c(k)$ is used, numerical problems might occur, for example in the computation of the pseudo inverse of $Y_{0,p,N}$ (see equation (4-25)) due to singularity.

The estimated model from the reduced data can be described as follows:

$$x(k+1) = A(k)x(k) + K(k)e(k), \tag{5-8}$$

$$c(k) = \bar{H}C(k)x(k) + \bar{H}e(k), \tag{5-9}$$

with $A(k) \in \mathbb{R}^{n_x \times n_x}$, $K(k) \in \mathbb{R}^{n_x \times \bar{n}_c}$ and $C(k) \in \mathbb{R}^{\bar{n}_c \times n_x}$.

Another advantage of the reduced model (5-8)-(5-9) is the fact that the constraint (5-3) is always satisfied. Hence, a KF will produce an estimate which satisfies the constraint (5-4). This is also known as the model reduction method [55].

Unfortunately, the estimation of the model (5-8)-(5-9) is not suitable for real-time control, because the vector $\bar{c}(k)$ is in general quite large. For example, if first order splines are used with zero order continuity (i.e. $d = 1$ and $r = 0$), then $\bar{n}_c$ is approximately equal to the amount of sub-apertures. Therefore the estimation of the model will be impossible for a high number of sub-apertures, even when the identification is done off-line.

5-2-2 Distributed CKF

With distributed CKF the domain of the WFR is divided into L different sub-domains. For each sub-domain a model can be estimated using the same method as described in the previous subsection. Therefore the following reduced vector of local coefficients is required:

$$c_i(k) = \bar{H}_i\bar{c}_i(k), i = 1, 2, \ldots, L. \tag{5-10}$$

Here, the index i refers to the number of the sub-domain. The vector $\bar{c}_i(k) \in \mathbb{R}^{\bar{n}_{c,i}}$ is the so-called local reduced data vector. The vector $c_i(k) \in \mathbb{R}^{n_{c,i}}$ contains the SABRE coefficients of the i-th sub-domain. The matrix $\bar{H}_i \in \mathbb{R}^{n_{c,i} \times \bar{n}_{c,i}}$ is an orthogonal basis of the null space of H_i and H_i is the matrix which contains the local constraints of the i-th sub-domain. With the local reduced data a model can be obtained:

$$x_i(k+1) = A_i(k)x_i(k) + K_i(k)e_i(k), \tag{5-11}$$

$$c_i(k) = \bar{H}_iC_i(k)x_i(k) + \bar{H}_ie_i(k). \tag{5-12}$$

Here $A_i(k) \in \mathbb{R}^{n_{x,i} \times n_{x,i}}$, $K_i(k) \in \mathbb{R}^{n_{x,i} \times \bar{n}_{c,i}}$ and $C_i(k) \in \mathbb{R}^{\bar{n}_{c,i} \times n_{x,i}}$ represent the local state, Kalman and output matrices respectively. These matrices can be estimated with Autonomous Predictor Based Subspace Identification (APBSID) (see section 4-3-2). Using the model (5-11)-(5-12), the predicted state can be computed using the following equations [47]:

$$\begin{aligned} \hat{x}_i(k+1|k) &= A_i(k)\hat{x}_i(k|k-1) + K_i(k)\left(\bar{c}_i(k) - C_i(k)\hat{x}_i(k|k-1)\right), \\ \hat{c}_i(k+1|k) &= \bar{H}_i C_i(k)\hat{x}_i(k+1|k). \end{aligned} \tag{5-13}$$

The to be predicted vector $\hat{c}(k+1|k)$ can be constructed by stacking all the local vectors, i.e.

$$\hat{c}(k+1|k) = \begin{bmatrix} \hat{c}_1^T(k+1|k) & \hat{c}_2^T(k+1|k) & \dots & \hat{c}_L^T(k+1|k) \end{bmatrix}^T.$$

In general, the constraints in (5-4) will not be satisfied, because the continuity constraints between two different sub-domains are not considered. The constrained estimate $\tilde{c}(k+1|k)$ can be computed by projecting $\hat{c}(k+1|k)$ onto the nullspace of the constraint matrix H. Another solution is to project the states $\hat{x}_i(k+1|k)$, such that we obtain directly the constraint estimate $\tilde{c}(k+1|k)$ using (5-13). This will be described in the following subsection.

5-2-3 State projection

The projected predicted state $\tilde{x}(k+1|k)$ satisfies the following constraint:

$$HC(k+1)\tilde{x}(k+1|k) = 0, \tag{5-14}$$

with

$$C(k) := \begin{bmatrix} \bar{H}_1 C_1(k) & 0 & \dots & 0 \\ 0 & \bar{H}_2 C_2(k) & \dots & 0 \\ \vdots & \vdots & \ddots & \vdots \\ 0 & 0 & \dots & \bar{H}_L C_L(k) \end{bmatrix}, \tag{5-15}$$

$$\tilde{x}(k+1|k) := \begin{bmatrix} \tilde{x}_1^T(k+1|k) & \tilde{x}_2^T(k+1|k) & \dots & \tilde{x}_L^T(k+1|k) \end{bmatrix}^T. \tag{5-16}$$

The constrained prediction can be computed in the following manner:

$$\tilde{x}(k+1|k) = \arg\min_x \left(x - \hat{x}(k+1|k)\right)^T W \left(x - \hat{x}(k+1|k)\right) \tag{5-17}$$

$$\text{s.t.} \quad HC(k+1)x = 0. \tag{5-18}$$

Here, $\hat{x}(k+1|k)$ is defined in an analogous way as $\tilde{x}(k+1|k)$ in (5-16) and $W \in \mathbb{R}^{n_x \times n_x}$ is a positive definite weighting matrix. If an identity matrix is used for the weighting matrix, then the mean square of $\tilde{x}(k+1|k) - \hat{x}(k+1|k)$ will be minimized. For minimal $\mathbf{E}\left[\left(x(k+1) - \tilde{x}(k+1|k)\right)\left(x(k+1) - \tilde{x}(k+1|k)\right)^T\right]$ the weighting matrix must be equal to the inverse of the error covariance matrix $W = P^{-1}(k+1|k)$ [54]. Here, $P(k+1|k)$ is defined as follows:

$$P(k+1|k) = \text{diag}\left(P_1(k+1|k), P_2(k+1|k), \dots, P_L(k+1|k)\right), \tag{5-19}$$

$$P_i(k+1|k) = \mathbf{E}\left[\left(x_i(k+1) - \hat{x}_i(k+1|k)\right)\left(x_i(k+1) - \hat{x}_i(k+1|k)\right)^T\right] \ \forall i = 1, \dots, L. \tag{5-20}$$

The analytic solution of (5-17)-(5-18) is given by

$$\tilde{x}(k+1|k) = \hat{x}(k+1|k) - W^{-1}\left(HC(k+1)\right)^T \left(HC(k+1)W^{-1}\left(HC(k+1)\right)^T\right)^{-1} HC(k+1)\hat{x}(k+1|k).$$

The required inverse of $HC(k+1)W^{-1}\left(HC(k+1)\right)^T$ can be a problem for real time application, because the dimensions of the matrix $HC(k+1)$ are proportional with the amount of sub-apertures. Because $C(k+1)$ depends on time, the inverse has to be computed at each time instant. However, due to the sparse structure of $HC(k+1)$ the problem (5-17)-(5-18) can be solved with distributive techniques. For example Alternating Direction Method of Multipliers (ADMM) is very well suited [8].

With the predicted state vector $\tilde{x}(k+1|k)$ the vector $\tilde{c}(k+1|k)$ can be computed using $C(k+1)$ from (5-15) as

$$\tilde{c}(k+1|k) = C(k+1)\tilde{x}(k+1|k).$$

Matrix $C(k+1)$ is a block-diagonal matrix, so this matrix-vector-multiplication is well suited for distributive techniques.

5-2-4 State projection with Piston Mode Equalization

As explained in section 3-3-2, the piston mode cannot be measured. Therefore an extra constraint is required, the so-called anchor constraint. This anchor constraint is only present in one of the L sub-domains. This implies that the piston mode for the other sub-domains needs to be predicted. This can be difficult, because the piston mode of one sub-domain also depends on the aberrations of other sub-domains. In order to model this correctly the number of states of x_i (i.e. n_x) could be large.

An alternative is to add an anchor constraint for each sub-domain, such that the piston mode is always equal. The anchor constraint can be defined as follows:

$$\begin{bmatrix} 1 & 0 & \dots & 0 \end{bmatrix} c_i(k) = h_i c_i(k) = 0. \tag{5-21}$$

In this example, the first coefficient is constrained, we could choose any coefficient. This constraint needs to be added to the local constraint matrix H_i. As a result, $\bar{H}_i$ will also change. If the anchor constraint is added, then the data $c_i(k)$ does in general not satisfy this constraint. Hence, $c_i(k)$ needs to be corrected:

$$c_i(k) = c_{i,\text{uncorrected}}(k) - \mathbb{1}_i z_i(k).$$

Here $\mathbb{1}_i \in \mathbb{R}^{n_{c,i}}$ is a vector that contains only ones, and z_i is the piston mode correction. If (5-21) is used as local anchor constraint, then $z_i(k)$ equals the coefficient of $c_{i,\text{uncorrected}}(k)$ which is constrained in (5-21).

If the piston mode is fixed for each sub-domain, then an extra step is required for the computation of the constrained estimate. The piston modes needs to be computed, which is called Piston Mode Equalization (PME) [16] and can be achieved by relaxation of the constraint in (5-18):

$$\{\tilde{x}(k+1|k), \alpha\} = \arg\min_{x,\alpha} \left(x - \hat{x}(k+1|k)\right)^T W \left(x - \hat{x}(k+1|k)\right) \tag{5-22}$$

$$\text{s.t.} \quad H\left(C(k+1)x + E\alpha\right) = 0. \tag{5-23}$$

Here $\alpha \in \mathbb{R}^L$ is a vector containing the piston modes for each sub-domain. The block-diagonal matrix E is defined as follows:

$$E = \text{diag}\left(\mathbb{1}_1, \mathbb{1}_2, \ldots, \mathbb{1}_L\right) \in \mathbb{R}^{n_c \times L}.$$

The predicted vector of coefficients can be computed as follows:

$$\tilde{c}(k+1|k) = C(k+1)\tilde{x}(k+1|k) + E\alpha.$$

5-2-5 State projection using ADMM

The dual ascent method is a well-known algorithm for solving optimization problems with linear constraints. If the functions can be decomposed, then the dual ascent method can be used to solve the problem in a parallel manner. Consider the problem of (5-17)-(5-18):

$$\min_x \left(\hat{x} - x\right)^T W \left(\hat{x} - x\right), \tag{5-24}$$

$$\text{s.t.} \quad H_x x = 0. \tag{5-25}$$

Here, the index $(k+1|k)$ of the vector $\hat{x}$ is omitted for brevity. Note that W and H_x may be time dependent and $H_x = HC(k+1)$, where for simplicity and without loss of generality it is assumed in this subsection that H only contains the global constraints, i.e. the constraints that addresses at least two coefficients of different sub-domains. It is assumed that the weighting matrix is a block diagonal matrix, i.e. $W = \text{diag}\left(W_1, \ldots, W_L\right)$. Therefore, the objective function (5-24) is decomposable.

In order to bring more robustness to the dual ascent method, an extra term is added to the minimization (5-24)-(5-25) resulting in the Method of Multipliers:

$$\min_x \left(\hat{x} - x\right)^T W \left(\hat{x} - x\right) + \frac{\rho}{2} \left\|H_x x\right\|_2^2, \tag{5-26}$$

$$\text{s.t.} \quad H_x x = 0. \tag{5-27}$$

where the parameter ρ is called the penalty parameter. The solution of (5-26)-(5-27) is equal to the solution of (5-24)-(5-25) as the extra term is zero if the constraint 5-27 is satisfied. Now let the Lagrangian be defined as follows:

$$L_\rho(x, y) = \left(\hat{x} - x\right)^T W \left(\hat{x} - x\right) + y^T \left(H_x x\right) + \frac{\rho}{2} \left\|H_x x\right\|_2^2, \tag{5-28}$$

where the vector y is the dual variable. With the Method of Multiplier the following algorithm is used to compute the optimum:

$$x^{k+1} = \arg\min_x L_\rho(x, y^k), \tag{5-29}$$

$$y^{k+1} = y^k + \rho H_x x^{k+1}. \tag{5-30}$$

Here, the index k denotes the iteration number. Equation (5-30) is called the dual update using the residual $H_x x^{k+1}$.

The idea of ADMM is to use the decomposability of the dual ascent method with the superior convergence properties of the Method of Multipliers. ADMM can be viewed as a version of

the Method of Multipliers where a single Gauss-Seidel pass over x_1, x_2, ..., x_L is used instead of the usual joint minimization (5-29) [8]. Now the optimization of (5-29) is decoupled into L smaller problems which have to be solved in sequence.

If the structure of H_x is taken into account, then the minimization of (5-29) can be decoupled into two minimizations, instead of L minimizations. This is a great improvement, because the two minimizations itself are very well suited for parallel programming. The key step is to rewrite the constraint (5-25) as follows:

$$H_{ij}\begin{bmatrix} x_i \\ x_j \end{bmatrix} = F_{ij}x_i + G_{ij}x_j = 0, \forall (i,j) \in \mathcal{E}. \tag{5-31}$$

Here, $\mathcal{E}$ is a set that contains all the combinations (i,j) such that the i-th sub-domain and the j-th sub-domain share an edge. The matrix H_{ij} contains the constraints that ensure the continuity between the i-th and j-th sub-domain. With (5-31), the Lagrangian (5-28) can be rewritten as follows:

$$L_\rho(x,y) = \sum_{i=1}^{L} (\hat{x}_i - x_i)^T W_i (\hat{x}_i - x_i) + \sum_{(i,j)\in\mathcal{E}} \left\{ (y_{ij})^T H_{ij} \begin{bmatrix} x_i \\ x_j \end{bmatrix} + \frac{\rho}{2} \left\| H_{ij} \begin{bmatrix} x_i \\ x_j \end{bmatrix} \right\|_2^2 \right\}. \tag{5-32}$$

Here, y is a vector in which all dual vectors y_{ij} with $(i,j) \in \mathcal{E}$ are stacked. Two methods which can be used to decouple (5-29) into two minimizations will be proposed.

ADMM with two subsets of sub-domains

This method can be used if the set of sub-domains can be separated into two subsets, such that one sub-domain has no neighboring sub-domain which is in the same subset. Let these two subsets be denoted with $\mathcal{X}$ and $\mathcal{Z}$. Without loss of generality, it can be assumed that H_{ij} is such that $i \in \mathcal{X}$ and $j \in \mathcal{Z}$. The minimization of (5-32) can be done in two steps: first, minimize (5-32) with respect to x_i $\forall i \in \mathcal{X}$ and second, minimize (5-32) with respect to x_j $\forall j \in \mathcal{Z}$. This method consists of the following iterations:

$$\begin{aligned}
\left\{ x_i^{k+1}, i \in \mathcal{X} \right\} &= \min_{x_i, i\in\mathcal{X}} \sum_{i\in\mathcal{X}} (\hat{x}_i - x_i)^T W_i (\hat{x}_i - x_i) + \\
&\qquad \sum_{(i,j)\in\mathcal{E}, i\in\mathcal{X}} \left\{ \left(y_{ij}^k\right)^T F_{ij}x_i + \frac{\rho}{2} \left\| H_{ij} \begin{bmatrix} x_i \\ x_j^k \end{bmatrix} \right\|_2^2 \right\}, \\
\left\{ x_j^{k+1}, j \in \mathcal{Z} \right\} &= \min_{x_j, j\in\mathcal{Z}} \sum_{j\in\mathcal{Z}} (\hat{x}_j - x_j)^T W_j (\hat{x}_j - x_j) + \\
&\qquad \sum_{(i,j)\in\mathcal{E}, j\in\mathcal{Z}} \left\{ \left(y_{ij}^k\right)^T F_{ij}x_j + \frac{\rho}{2} \left\| H_{ij} \begin{bmatrix} x_i^{k+1} \\ x_j \end{bmatrix} \right\|_2^2 \right\}, \\
y_{ij}^{k+1} &= y_{ij}^k + \rho H \begin{bmatrix} x_i^{k+1} \\ x_j^{k+1} \end{bmatrix} \forall (i,j) \in \mathcal{E}.
\end{aligned}$$

Note that both minimizations have to be done in sequence, but that the minimizations itself are very suitable for parallel programming. This is a result from the fact that for any $i \neq k$ with $i \in \mathcal{X}$ and $k \in \mathcal{X}$ we have $(i,k) \notin \mathcal{E}$. With the same reasoning it follows that for any $j \neq k$ with $j \in \mathcal{Z}$ and $k \in \mathcal{Z}$ we have $(j,k) \notin \mathcal{E}$.

ADMM with Coupling Vectors

With the second method a relaxation of the problem (5-26)-(5-27) is used. The idea is to write the constraint (5-31) as follows [56]:

$$F_{ij}x_i = z_{ij}, \forall (i,j) \in \mathcal{E},$$
$$G_{ij}x_j = -z_{ij}, \forall (i,j) \in \mathcal{E}.$$

Here, z_{ij} are the so-called coupling vector. With these constraints the Lagrangian will be

$$\begin{aligned} L_\rho\left(x, y_f, y_g, z\right) = &\sum_{i=1}^{L} \left(\hat{x}_i - x_i\right)^T W_i \left(\hat{x}_i - x_i\right) + \\ &\sum_{(i,j)\in\mathcal{E}} \left\{ \left(y_{ij,f}\right)^T \left(F_{ij}x_i - z_{ij}\right) + \frac{\rho}{2} \left\| F_{ij}x_i - z_{ij} \right\|_2^2 \right\} + \\ &\sum_{(i,j)\in\mathcal{E}} \left\{ \left(y_{ij,g}\right)^T \left(G_{ij}x_j + z_{ij}\right) + \frac{\rho}{2} \left\| G_{ij}x_j + z_{ij} \right\|_2^2 \right\}. \end{aligned}$$

Here, all $y_{ij,f}$ with $(i,j) \in \mathcal{E}$ are stacked in the vector y_f. The vectors y_g and z are defined in an analogue way. With the following iterations the problem can be solved:

$$\begin{aligned} x^{k+1} &= \min_x L_\rho\left(x, y_f^k, y_g^k, z^k\right) \\ z^{k+1} &= \min_z L_\rho\left(x^{k+1}, y_f^k, y_g^k, z\right) \\ y_{ij,f}^{k+1} &= y_{ij,f}^k + \rho\left(F_{ij}x_i^{k+1} - z_{ij}^{k+1}\right) \forall (i,j) \in \mathcal{E} \\ y_{ij,g}^{k+1} &= y_{ij,g}^k + \rho\left(F_{ij}x_i^{k+1} - z_{ij}^{k+1}\right) \forall (i,j) \in \mathcal{E} \end{aligned}$$

The constraint 5-25 can be seen as the coupling between the different sub-domains. The coupling vectors can be seen as the connection between the sub-domains. Therefore, the first step of the algorithm is very suitable for parallel programming: because of the use of the coupling variables the state x_i is decoupled from the state x_j for any $j \neq i$. Note also that the minimization with respect to a coupling vector is independent of other coupling vectors. Hence, this can also be done in a parallel manner.

Remarks

The two aforementioned methods are both suitable for parallel programming. Both methods have advantages and disadvantages:

- The disadvantage of the second method (i.e. the method with the coupling vectors) is that due to the relaxation more iterations are required with respect to the method in which the sub-domains are separated into two subsets. Because more optimization variables (i.e. the coupling vectors) are involved, the number of iterations increases [56].
- The first method requires two steps in which the Lagrangian is minimized with respect to local vectors. With the second method, the Lagrangian can be minimized with

respect to all the local states at the same time, however, an extra minimization with respect to the coupling vectors is required. If the minimization with respect to the local states takes longer than the minimization with respect to the coupling variables, then the second method might be faster. This depends much on the size of the local states.

- A disadvantage of the first method is the fact that it must be possible to divide the set of all sub-domains into two subsets of sub-domains, such that two sub-domains of one subset cannot be neighboring sub-domains (i.e. they cannot share an edge). This limits the possibilities for defining the sub-domains.
- Both methods have the advantage that the minimizations can be done analytically. Each minimization requires an inversion of a matrix, but this has to be done once per time instance. If this is done, then each ADMM iteration only requires a matrix-vector-multiplication.

5-3 Experiments with Yao

In this section, simulations are performed to investigate if the (C)KF improves the prediction of the aberrations compared to the delayed reconstruction. Subsection 5-3-1 gives a description of the experiments. Subsections 5-3-2, 5-3-3 and 5-3-4 describe how the sample time, systems orders and future/past windows are chosen, respectively. In subsection 5-3-5, different weighting matrices W are tested. Subsection 5-3-6 shows the difference between the results of the KF and the CKF. In the final subsection, the state projection with PME is tested.

5-3-1 Description of experiments

Spline based ABerration REconstruction (SABRE) is used to reconstruct the wavefront aberrations of an Adaptive Optics (AO) system (see section 3-3). For a more detailed description of AO, see chapters 1 and 3 of this thesis. In the experiments the AO system will be open-loop, i.e. there will be no Deformable Mirror (DM).

Yorick is used for the simulations in combination with Yao. See section 3-4-1 for a description of Yorick and Yao. Also the parameter of the telescope and wavefront aberrations can be found in section 3-4-1.

A Shack-Hartmann (SH) sensor with 6×6 sub-apertures is used for the reconstruction. The intensity measurements are disturbed by two types of noise: photon noise with a Poisson distribution and read-out noise with a Gaussian distribution. The read-out noise has a mean of zero and a standard deviation of 3.5 electrons per pixel.

Each experiment consist of two stages. The first stage, only consists of reconstructing the wavefront using SABRE. With the data from this stage the local systems are identified using Autonomous PBSID (APBSID) (see section 4-3-2). In the second stage, the (C)KF is tested where the initial state is computed from the data from the first stage. The amount of data samples for the first stage determines how accurate the identification of the local system descriptions will be. Too much data will lead to very large computational times, so therefore

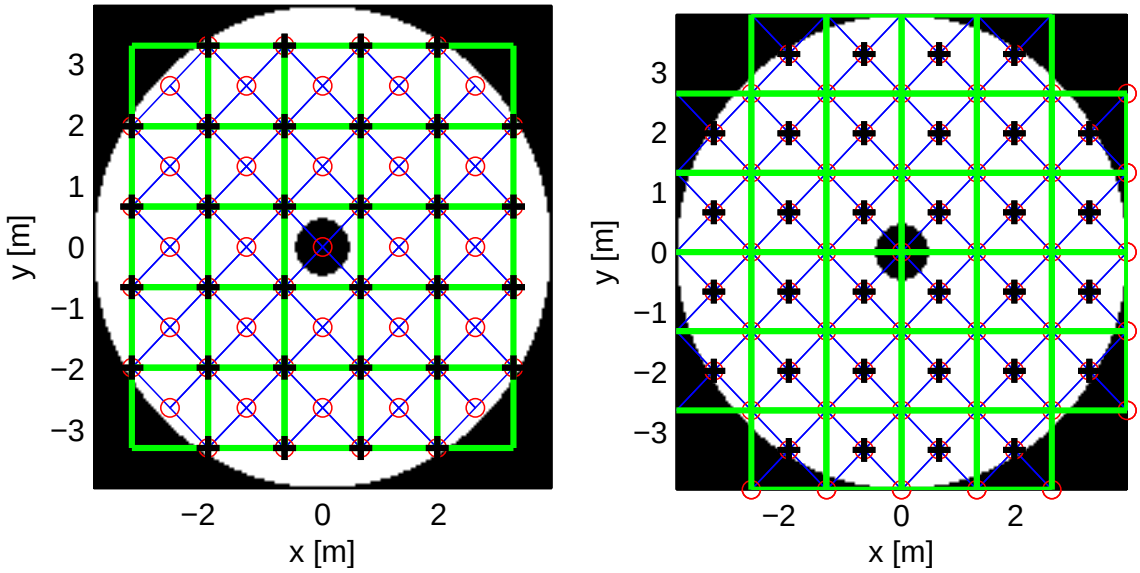

(a) Gradient based SABRE **(b)** Intensity based SABRE

Figure 5-1: Triangulation and sub-domains for (a) gradient based SABRE and (b) intensity based SABRE. The black area represent the area which is not illuminated. The blue lines represent the edges of the triangles. The red circles are the vertices of these triangles. The borders of the sub-domains are shown by the green lines. The centers of the sub-apertures are represented by the black crosses.

a compromise needs to be found. The results are not further improved when using more than 1600 data samples, so this is the amount of data samples which will be used for the first stage. For the second stage 1000 data samples are used. If not otherwise mentioned, then the CKF will be used without PME.

The order of degree of the reconstructed aberrations are equal to $d = 1$ and the order of continuity will be $r = 0$. A type II triangulation will be used. The definition of the triangles are different for intensity based SABRE when compared with gradient based SABRE. Therefore also the sub-domains are differently defined. Each square will be a sub-domain, as can be seen in figure 5-1. In figure 5-1, the triangulations of both methods is shown. The green lines represent the edges of the sub-domains. As can be seen with gradient based SABRE there will be 25 sub-domains en with intensity based SABRE there will be 32 sub-domains.

The goal of the WFR and KF is to estimate the aberrations as accurate as possible, i.e. the variance of the error has to be minimized. Therefore the performance indicator of (3-39) can be used to see how the KF performs. However, the influence of the KF and the corresponding parameters which can be tuned do not have a very significant influence on the performance P of (3-39). Hence, a new performance indicator has to be introduced:

$$R = \frac{\mathbf{E}\left[P(k|k) - P_{KF}(k|k-1)\right]}{\mathbf{E}\left[P(k|k) - P(k|k-1)\right]} 100\%. \tag{5-33}$$

Here, the time index $k|j$ refers to the performance of the WFR with data of time instant j with respect to the aberration at time instant k. The index KF refers to the fact that the

performance indicator is computed of the predicted aberration using the KF with data up to the indicated time index. In formula's we have:

$$P(k|j) = \frac{RMS(\varphi(k) - \phi(j))}{RMS(\varphi(k))} 100\%,$$
$$P_{KF}(k|j) = \frac{RMS(\varphi(k) - \phi_{KF}(j+1|j))}{RMS(\varphi(k))} 100\%,$$

with $\phi(k)$ denoting the estimated aberration using the data of time instant k and $\phi_{KF}(k+1|k)$ denotes the prediction of $\varphi(k+1)$ using the wavefront reconstructions up to time instant k. Note that $\mathbf{E}[\cdot]$ denotes the expectation operator. As mentioned earlier, the second stage consists of 1000 data samples, so the expectation is approximated by the mean over those 1000 samples.

Although the denominator of R can theoretically be negative, it is practically always positive. That implies that a lower value of R means a better performance of the (Constrained) Kalman Filter. If $R \geq 100\%$, then the predicted wavefront $\phi(k|k-1)$ of the (C)KF does not give a better result than the delayed reconstruction $\phi(k-1)$, so if $R < 100\%$, then the (C)KF improves the prediction. If $R < 0\%$, then the predicted aberration $\phi(k|k-1)$ is even better than the estimated aberration using data of time instant k, i.e. $\phi(k)$.

5-3-2 Choosing the sample time

Greenwood [4] pointed out that for worst case conditions the cut-off frequency of the wavefront aberrations is at $172Hz$. As a rule of thumb the sample frequency should be one order higher than the cut-off frequency. Hence, a sample time of about $0.5ms$ to $1ms$ can be considered when this worst case scenario is considered.

In order to determine the sample time a closer look to the experiments is used. In figure 5-2, the smoothed Fourier transforms of different coefficients are shown. These coefficients are calculated using gradient based SABRE. At low frequencies, the modulo is approximately $50dB$. For frequencies higher than $250Hz$, the modulo is lower than $10dB$ which is $40dB$ lower than $50dB$. If it is assumed that the higher frequencies can be neglected, then a sample frequency of $500Hz$ is good. Hence, a sample time of $2ms$ is chosen for all the experiments.

5-3-3 Choosing the system order n

For the identification, APBSID is used (see section 4-3-2). The singular values of the SVD of equation (4-22) give insight for choosing the order of the system. The system order can be found by detecting a gap that separates the n largest singular values. It is observed that for any sub-domain there is a gap after the n-th largest singular value, such that n is the size of the local reduced vector of coefficients.

As an example, in figure 5-3, the singular values are plotted for one sub-domain. Also the difference is shown when using PME or not. In order to see any difference in the singular values between using PME or not, the sub-domain which is used is on the opposite side of focal plane compared to the sub-domain which contains the global anchor constraint (3-23). The sub-domain which is used in figure 5-3 contains four simplices. Hence, 12 coefficients

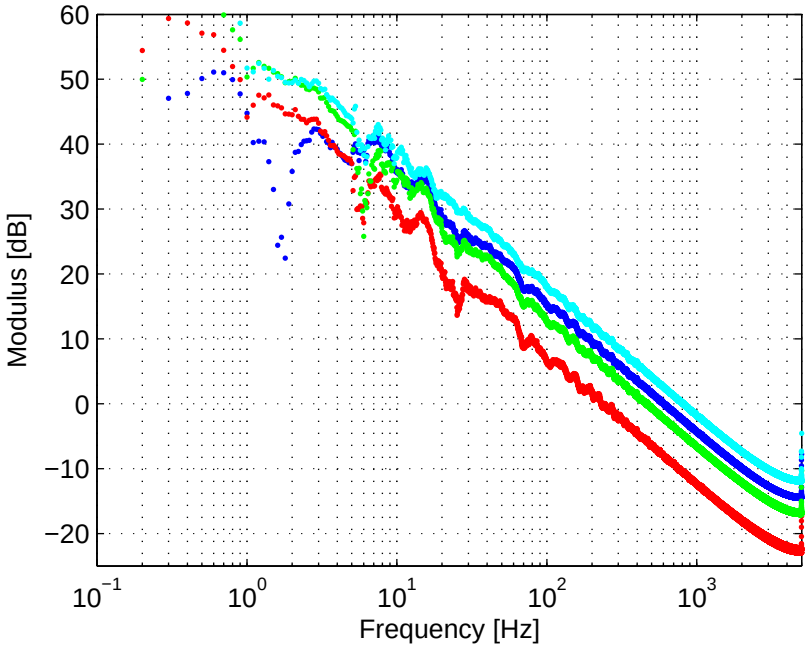

Figure 5-2: Smoothed Fourier transform of different coefficients from the SABRE. The modulus is decreasing with $20dB/dec$.

are used to define the phase within this sub-domain. The sub-domain contains seven local constraints. Hence, the local reduced data vector $\bar{c}_i(k)$ contains five entries. Note that this is independent of the method (i.e. the gradient or intensity based method) which is used for reconstruction. For the particular sub-domain used in figure 5-3 there is a gap after the fifth singular value when PME is not used. When PME is used a gap can be seen after the fourth singular value. This also equals the size of the local reduced data vector, since this vector has four entries when PME is used.

The system order of each sub-domain will be equal to the number of entries of the local reduced data vector. Figure 5-3 shows that this is correct for that particular sub-domain. Although it is not shown here, the other sub-domains show the same behavior: a gap that separates the first n singular values, where n is the amount of entries of the local reduced data vector. An advantage of using the same order as the amount of entries of the local reduced data vector is the fact that it is easy to determine the order of a system. There is no need for an algorithm which searches for a gap between two singular values, since the amount of entries is always known.

5-3-4 Influence of past and future windows p and f

APBSID is used for the identification of the local state space description. Besides choosing the order n of the local systems, also the past and future windows needs to be chosen. In section 4-4-2, the effect of past window p and future window f is described. In figure 5-4, the effect of p and f on the result R is shown for this particular experiment.

In case of gradient based SABRE, a future window of only one gives already good results.

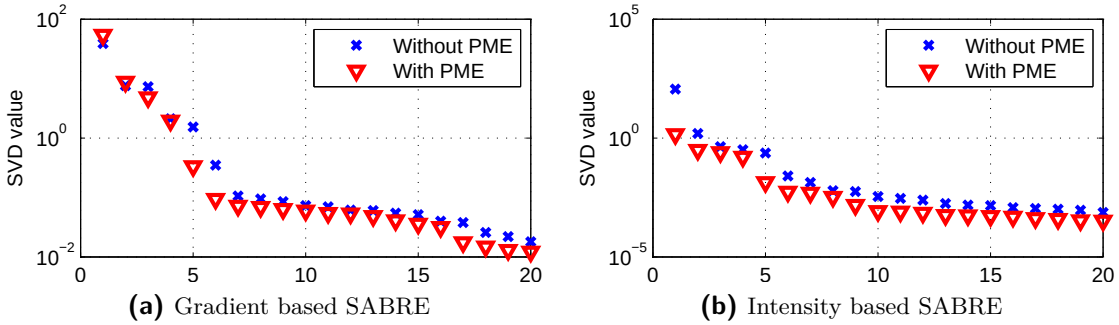

(a) Gradient based SABRE **(b)** Intensity based SABRE

Figure 5-3: The singular values of $W\tilde{\mathcal{O}}_f\tilde{\mathcal{K}}_pY_{0,p,N}$ (see equation (4-29) in subsection 4-3-2) in decreasing order.

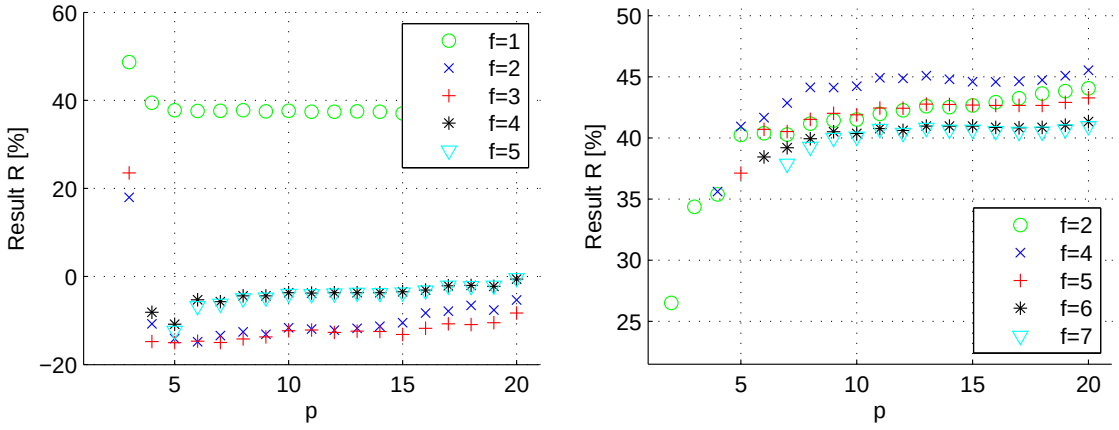

(a) Gradient based SABRE **(b)** Intensity based SABRE

Figure 5-4: Results (5-33) of the experiments for different future and past windows, denoted by f and p respectively.

However, a future window of 2 or higher gives comparably better results. From figure 5-4a, it can be seen that p does not have a large influence on the result. The best results are obtained with $p = 5$. For $p > 5$ the result R is slightly increasing. From figure 5-4a, it appears that with $f = 2$ and $f = 3$ the best results are obtained. For the next experiments $f = 3$ and $p = 5$ will be used when gradient based SABRE is used for the WFR.

The influence of p and f on the result R when intensity based SABRE is used is shown in figure 5-4b. In this figure, the results obtained with $f = 1$ and $f = 3$ are not shown, because it resulted in very large values of R. The bad results were caused by the estimated matrix $A - KC$, which was instable for one or more sub-domains. As long as $f \neq 1$ and $f \neq 3$ the results are good. The best result is obtained with $f = 2$ and $p = 2$, so these values will be used when intensity based SABRE is used for the WFR.

5-3-5 Influence of weighting matrix W

In order to make sure that the states satisfy the continuity constraint (5-14) the state projection method is used. As described in subsection 5-2-3, a positive definite weighting matrix W can be used for the state projection. In this subsection different choices of W are compared:

1. $W_1 = I$;
2. $W_2 = C^T(k)C(k)$;
3. $W_3 = \text{diag}\left(P_1^{-1}, \ldots, P_L^{-1}\right)$ with $S_i = 0$, $Q_i = I$ and $R_i = I$.

If the weighting matrix is equal to the identity matrix, then the 2-norm of the difference between the unconstrained and constrained state (i.e. $\hat{x} - \tilde{x}$) is minimized.

The goal of the KF is to estimate $c(k+1|k)$, i.e. the estimate of the SABRE coefficient for the next time instant. W can be chosen such that $\hat{c}(k+1|k) - \tilde{c}(k|1|k)$ is minimized. Then W has to equal the second choice, i.e. $W = W_2$. However, this can lead to a singular weighting matrix if a local output matrix has more columns than rows, i.e. if $\bar{n}_{c,i} < n_{x,i}$ for $i \in 1, \ldots, L$. As explained in subsection 5-3-3 in our case $\bar{n}_{c,i} = n_{x,i}$, so W is non-singular if all the local output matrices are full rank. Note that a combination of W_1 and W_2 is also possible, so for example $W = W_1 + \alpha W_2$ for some positive α. In that case the weighting matrix is always positive definite.

For minimal variance of error between the real and the predicted state, the weighting matrix should be equal to the inverse state covariance matrix [54] and defined in (5-19)-(5-20). Hence, this would give the optimal results. Unfortunately, this state covariance matrix is unknown. Therefore it is computed by solving the discrete algebraic Riccati equation:

$$P_i = A_i P_i A_i^T + Q_i - \left(S_i + A_i P_i C_i^T\right)\left(R_i + C_i P_i C_i^T\right)^{-1}\left(S_i + A_i P_i C_i^T\right)^T.$$

Here the local noise covariance matrices are unknown, and thus $S_i = 0$, $Q_i = I$ and $R_i = I$ are used.

In table 5-1, the results of the CKF are shown for different weighting matrices. With gradient based SABRE, the second choice, i.e. $W = W_2$, gives the best result. Theoretically, $W = W_3$

Table 5-1: Results for different choices of the weighting matrix W for gradient and intensity based SABRE.

W	Gradient based SABRE [%]	Intensity based SABRE [%]
$W = W_1$	6.961	27.33
$W = W_2$	-16.95	27.40
$W = W_3$	-14.07	27.23

Table 5-2: Comparison of the results of the CKF and the unconstrained KF. The CKF performs better than the unconstrained KF with gradient based SABRE. With intensity based SABRE using the CKF does slightly decrease the performance.

	Result with KF [%]	Result with CKF [%]
Gradient based SABRE	28.20	-16.95
Intensity based SABRE	26.57	27.23

should give the best results if the right covariance matrices were used, but these covariance matrices are unknown and therefore the result with $W = W_3$ is only slightly worse compared to the result with $W = W_2$. With intensity based SABRE, the method performs equally well for the different weighting matrices.

5-3-6 Constrained Kalman Filtering versus Kalman Filtering

In table 5-2, the results of using a CKF or an unconstrained KF are shown. With the unconstrained KF the state projection of (5-17)-(5-18) is not applied. With the CKF the weighting matrix W is used which gave the best result, i.e. $W = W_3$ for intensity based SABRE and $W = W_2$ for gradient based SABRE.

With gradient based SABRE the result with CKF is better compared to the result with the unconstrained KF. The result with the CKF is $R = -16.95\%$, which implies that the CKF predicts the aberration $\varphi(k+1)$ at time instant k even better than the reconstruction at time instant $k+1$, i.e. $\phi(k+1|k)$ is a better estimate of $\varphi(k+1)$ than $\phi(k+1)$.

We observe that with gradient based SABRE the CKF predicts the aberration significantly better than the unconstrained KF. This could be explained as follows: the KF predicts the aberration such that the continuity constraints between two different sub-domains does not have to be met, while the CKF predicts a continuous aberration. This implies that the range of possible solutions of the KF is much larger than the range of possible solutions of the CKF. Hence, also the prediction error variance of $\hat{x}(k+1|k)$ will be larger than the prediction error variance of $\tilde{x}(k+1|k)$.

With intensity based SABRE, there is not a significant difference between the results: with CKF we have $R = 27.23\%$ and with the unconstrained KF we have $R = 26.57\%$, which is slightly better. This seems to be unexpected, as the CKF should give a lower variance of the prediction error of the local states. However, the the performance indicator R gives an

Table 5-3: Results for different choices of the weighting matrix W for gradient and intensity based SABRE with PME.

W	Gradient based SABRE [%]	Intensity based SABRE [%]
$W = W_1$	72.08	384.0
$W = W_2$	68.66	370.1
$W = W_3$	68.99	372.2

indication how well the predicted aberration is, compared with the real aberration. Because of the continuity constraints, the range of possible reconstructions is highly reduced, which is a disadvantage. But the advantage of this is that the problem is better defined, which can improve the result, e.g. if there is much measurement noise. So with intensity based SABRE the advantage for having a larger range of solutions is slightly larger than the disadvantage of having a higher variance of the prediction error of the local states.

5-3-7 State projection with Piston Mode Equalization

In table 5-3, the results are shown for the CKF with PME as described in subsection 5-2-4 for different weighting matrices W. The weighting matrices W_1, W_2 and W_3 are defined in subsection 5-3-5. As can be seen in table 5-3, the results are worse compared to the results without PME (see table 5-1). If the CKF is used without PME, then the local piston modes are predicted by the local estimated models. If PME is used, then these piston modes are not predicted, but computed during the state projection. This will give a better result if the local estimated models do not model the local piston modes correctly. From the results it can be concluded that it is better to predict the local piston models, i.e. to not use the state projection with PME.

5-4 Conclusion

The goal of this chapter was to find a filter which produces a better estimate for $\varphi(k+1)$ than the delayed reconstruction $\phi(k)$, where SABRE is used for the WFR. For this purpose a (C)KF is used. It has been shown that the estimated aberrations (i.e. $\phi(k+1|k)$ are better than the delayed reconstruction (i.e. $\phi(k)$). In some cases the estimated aberration $\phi(k+1|k)$ gave even better results than the reconstruction at time instant $k+1$ (i.e. $\phi(k+1)$).

Many parameters do influence the (C)KF, for example the sample rate, the local system orders, the past window (i.e. p), the future window (i.e. f) and the weighting matrix for the state projection (i.e. W). It is shown how the sample rate and the local system orders are chosen. Also the effect on the result of past and future windows is shown. Three different weighting matrices are compared.

With the experiments it is shown that using a CKF instead of a KF improves the result when gradient based SABRE is used. With intensity based SABRE the difference between the results of the CKF and KF were very small. From the experiments it can be concluded that

CKF with PME does not improve the results. Most importantly, it has been demonstrated that a (C)KF predicts the aberrations more accurate compared to the delayed reconstruction and at times even outperform the reconstruction without delay.

Chapter 6

Conclusions and Recommendations

6-1 Conclusions

In this thesis, it is shown that Spline based ABerration REconstruction (SABRE) with intensity measurements can be used to reconstruct the wavefront in real-time where a Shack-Hartmann (SH) sensor is used as Wavefront Sensor (WFS). Furthermore, is has been demonstrated that with Subspace Identification (SID) and a Kalman Filter (KF) the performance improves even further.

The performance of intensity based SABRE has been compared with the performance of gradient based SABRE with the Adaptive Optics (AO) simulation tool Yao and a SABRE library, which is written as part of this graduation project. An extra measurement under the same blurring conditions but which an additional defocused aberration is used for avoiding non-unique solutions.

From the experiments it could be concluded that the intensity based SABRE performs better than the gradient based SABRE with small aberrations. In the experiments with Yao, the intensity based SABRE performs better when $r_0 \geq 1m$ where r_0 denotes the Fried parameter. In astronomy, the Fried parameter r_0 varies from $0.05m$ to $0.4m$, so gradient based SABRE will perform better.

The experiment demonstrated that intensity based SABRE is more robust to sensor noise of the SH WFS with respect to gradient based SABRE. Due to the sensor noise, the WFR can become worse if more sub-apertures are used, because with more sub-apertures each sub-aperture will be less illuminated and therefore the signal to noise ratio will decrease. This effect is also observed with gradient based SABRE. With intensity based SABRE, however, this has not been observed, because of the increased noise robustness. Hence, it could be concluded that with intensity based SABRE this effect of having a worse wavefront reconstruction with more sub-apertures, will only occur at a much larger number of sub-apertures when compared to gradient based SABRE.

In order to obtain a model of the temporal dynamics, two Autonomous Subspace Identification (ASID) methods are presented: Past Output ASID (PO-ASID) and Autonomous Predictor

Based Subspace Identification (APBSID). Both methods are closely related to already existing SID methods. It is shown that both methods give unbiased results. APBSID is used to model the temporal dynamics of the aberrations, because with APBSID also the Kalman gain is estimated, which is used for the KF.

Estimating the temporal dynamics for the whole system would take too much time, so the whole domain has been partitioned into sub-domains, which is uncomplicated because of the local nature of SABRE. SID is applied for each sub-domain to obtain a local model description. The identification of the model of one sub-domain can be performed independently of other sub-domains, so this can be done in a parallel manner.

The estimated local model descriptions are used for the Kalman Filter (KF) to predict the local state update, i.e. the local state for the next time step. Predicting the local state update of one sub-domain can be done independently of other sub-domains, so it can be done in a distributive manner. From this local state update the SABRE coefficients of the next time step could be predicted. Combining the SABRE coefficients of all sub-domains gives an estimate of the aberration of the next time step. Because SABRE is used, constraints can be used to ensure a certain order of continuity between two neighboring sub-domains, which motivated the use of a Constrained Kalman Filter (CKF). If the local states are corrected such that these continuity constraints are satisfied, then the prediction of the aberration is further improved. This is done with a state projection, which is suitable for parallel programming. We presented two distributive algorithms, which can be used to perform the state projection in a distributive manner. Both methods use the Alternating Direction Method of Multipliers (ADMM).

The prescribed CKF is tested in a simulation in Yorick, which is a programming language for steering large scientific simulation codes. The AO system is simulated using the plugin Yao. Besides, the prescribed (C)KF and SID have been programmed in Yorick. With these experiments the choices of the sample time, local system orders, future and past windows have been motivated. With the CKF different weighting matrices can be defined and these different weighting matrices are also compared in the simulations.

In the simulations, it is demonstrated that the distributed SID and the distributed KF improve the predictions of the aberrations significantly compared to the delayed reconstructions. Moreover, if the reconstruction is not delayed, then with gradient based SABRE, the prediction still outperforms the reconstruction.

In this thesis it is shown that intensity based SABRE performs better than the traditional methods when used to reconstruct the wavefront with data from a SH WFS, although the aberrations should not be too high. Furthermore, a method is presented for the prediction of the aberration using a KF and SID. The method exploits the local nature of SABRE, such that it is suited for parallel programming. In experiments it has been demonstrated that the estimation of the aberration is significantly improved with the (C)KF by compensating for the delay.

6-2 Recommendations & Future work

During my research, I did some interesting observations, which could possibly lead to improvements, although they were out of the scope of this thesis. However, with future research, these recommendations could be taken into account.

- The experiments can also be done in closed loop, i.e. with a Deformable Mirror (DM). The goal of AO is to correct for the aberrations, such that the variance of the residual aberration is as small as possible. In this thesis, it has been demonstrated that the (C)KF give good predictions of the aberrations, but the correction with a DM is not applied. It would be useful to see how much the performance of an AO system is improved when using the (C)KF to predict the aberrations.

- In order to demonstrate the usefulness of the KF it was necessary to have a model description of the temporal dynamics and therefore ASID was used. In the simulations these temporal dynamics were not changing over time, but this is in general not the case. Therefore Recursive ASID can be used. Note that the presented (C)KF is also applicable in real-time if Recursive ASID is used. Houtzager et al. [51] present a recursive implementation of PBSID, which can be adapted such that it can be used for the Recursive ASID. The method proposed by Lovera et al. [57] can be used to adapt PO-ASID for a recursive implementation.

- Two important parameters of SABRE are the degree of the polynomial (denoted by d) and the degree of continuity (denoted by r). In this thesis only the pair $(d, r) = (1, 0)$ is considered, but this is not optimal in all cases [6, 56].

- The simulations has been performed on a single CPU. However, SABRE is very applicable for parallel programming [16, 56]. Also the (C)KF is suitable for parallel programming, for example with the use of ADMM [8] (see subsection 5-2-5). It would be useful to program the algorithms in a parallel manner. First, this will probably give more insight in how well these methods perform in terms of speed. Second, then it is also possible to do more experiments, because now the computational time is limiting the amount of experiments.

- We observed with the comparison of the (C)KF and the KF that the continuity constraints does not necessarily lead to better results (see subsection 5-3-6). With the unconstrained KF the continuity constraints between different sub-domains are not considered and with the CKF the continuity constraints are strictly met. However, a compromise is also possible with soft constraints. When ADMM is used for the state projection, then the soft constraints could be applied by limiting the amount of iterations. The soft constraints can be applied for the WFR and the CKF.

Appendix A

Simulations with Yao

Yao is used for the simulations of chapter 3 and chapter 5. In this appendix yao is shortly described. There are some functionalities added, for example to perform Spline based ABerration REconstruction (SABRE). For future work it might be useful if there is some documentation, so this is also a reason for this appendix.

This appendix has the following lay-out. First it is explained what Yao actually is. In A-2 it is explained why Yao is used for the simulations of this thesis. In A-3 and A-4 the extra functionalities concerning SABRE and Subspace Identification (SID) respectively will be described. In section A-5 some future work is listed.

A-1 What is Yao?

Yao is an open-source Adaptive Optics (AO) simulation tool which simulates a number of aspects of AO [44]. Some highlight of yao are:

- The aberrations are modeled in Yao according to the Kolmogorov model. Different wind speeds and layers can be defined. The amount of turbulence can be changed easily.
- It models different wavefront sensors, for example the Shack-Hartmann (SH) Wavefront Sensor (WFS).
- Different deformable mirrors can be used, for example the Stackarray and Tip-Tilt.

Yao is mainly programmed in Yorick. Yorick is an interpreted programming language for scientific simulations or calculations, postprocessing or steering large simulation codes [43]. Yorick is also open-source. Some parts of Yao have been coded in C, which improves the execution time of the simulation. Furthermore yao can be used in parallel mode, using the yorick svipc plugin.

The experiments with yao can be configured using the large list of parameters. These parameters are explained in the manual of yao (http://frigaut.github.io/yao/manual.html).

In figure A-1 an example of the plots which yao produces is shown.

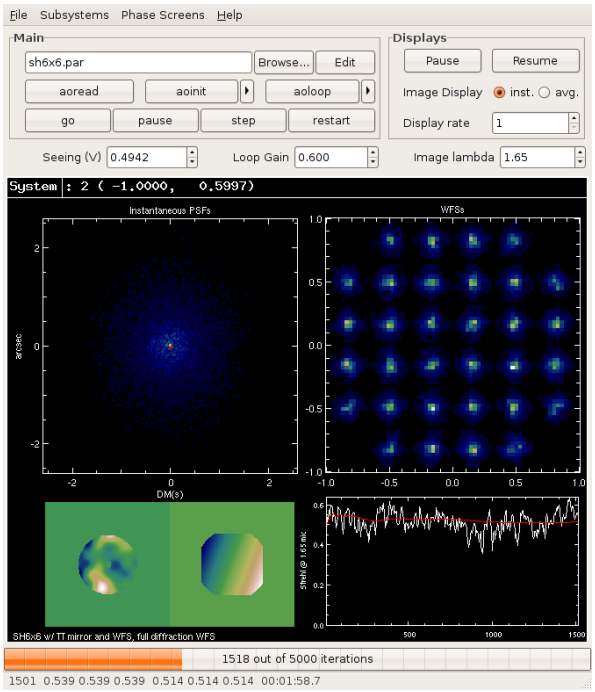

Figure A-1: Image of the figures produced by yao. In the top left corner the instant Point Spread Function (PSF) is shown. Below the PSF the Strehl ratio is plotted over time. The black (red) line represent the short (long) term Strehl ratio. In the left bottom corner the two DMs are shown. In this case the Stackarray and Tip-Tilt DMs are used. An image of the SH WFS is shown in the top right corner. Right bottom corner shows the residual wavefront.

A-2 Why Yao?

The AO simulations of this thesis are performed with Yao. The first reason to use yao is simply because it is an AO simulation tool. Coding an AO simulation tool consumes much effort. Secondly, it is open-source; hence it is free to use. Thirdly yao is updated semi-regularly.

A-3 SABRE

A library has been written in order to make it possible to reconstruct the wavefront using SABRE. Gradient based SABRE and intensity based SABRE are possible. The most important features are the initialization, reconstruction and evaluation. The initialization can take much time; therefore it is possible to store the results from the initialization for other experiments.

During the initialization the reconstruction matrix Q is computed. This matrix Q is such that the estimated SABRE coefficients $\hat{c}_{LLS}$ can be computed using a matrix-vector multiplication:

$$\hat{c}_{LLS} = Q\sigma. \tag{A-1}$$

Here σ is the vector that contains the measurements. When gradient based SABRE is used this vector contains the measured gradients and for intensity based SABRE this vector contains the difference of the measured intensities and c_0. The reconstruction consists of two matrix-vector multiplications. The first multiplication is used to compute the SABRE coefficients, see (A-1). With the second multiplication the estimated aberration is computed from the SABRE coefficients, according to (3-17). The required matrix $\mathbf{B}^d$ is computed during the initialization. The evaluation is done using (3-39). The performance indicator P is used to measure how well the estimated aberration is compared to the real aberration.

Part of the SABRE library is the possibility to use a Kalman Filter (KF). This has been written in the SABRE library, because the (Constrained) KF is adapted for this use. Table A-2 lists the options which can be changed during the initialization of the KF. Also the parameters that are important for the Subspace Identification (SID) are listed in this table. More details of the corresponding functions can be found in the documentation of the code.

A-4 SID

In order to obtain a model, which can be used by the KF, Subspace Identification (SID) is used. Therefore, as part of the project, different function are programmed in Yorick. The following SID methods are available:

- Predictor Based Subspace Identification (PBSID);
- Autonomous PBSID (APBSID);
- Recursive APBSID (RAPBSID). RAPBSID needs to be initialized first.

Table A-1: List of parameters which needs to be defined before the initialization of the SABRE

Parameter(s)	Comment
`ns`	The number of WFS which is used for the reconstruction. Of course this WFS needs to be defined. In theory it is also possible to use two WFSs, but this is not supported.
`TRIype`	The type of triangulation determine how the domain is split into different simplices. In this thesis only triangulation type I and II are considered.
`d`,`r`	`d` and `r` are the order of degree and the order of continuity respectively. In this thesis the combination $d = 1$ and $r = 0$ is the only combination which is considered. Other combinations are not yet supported.
`method`	With this parameter the method can be defined. This can be gradient based SABRE (`method='gradient'`) or intensity based SABRE (`method='intensities'`).
`dcoef`	The computation of the Jacobian matrix C_1 (3-36) is done with a finite difference method. `dcoef` is the stepsize which will be used. This parameter can be omitted if gradient based SABRE is used.
`defocus_method`	If a defocus is used, then `defocus_method` defines which type of defocus. This can be `1` or `2`, see figure 3-1 for the definition of the different types of defocus. This parameter can be omitted if gradient based SABRE is used.
`defocus`	This parameter defines the amount of the defocus, see section 3-3-3 for an explanation. If `defocus=0` then no defocused image will be used. This parameter can be omitted if gradient based SABRE is used.

Table A-2: List of parameters relating to Subspace Identification (SID) and Kalman Filter (KF), which can be defined before the initialization of SABRE

Parameters(s)	Comment
`p`,`f`	Past and future window. See section 4-4-2 and 5-3-4 for an detailed description.
`n_per_c`	This determines the ratio of the order of the local state space descriptions and the number of coefficients of the local reduced data vector (i.e. $\bar{n}_c$).
`PME`	Set to `1` if the state projections should be done with Piston Mode Equalization (PME) (see subsection 5-2-4 for a description of the PME). Default is `0`.
`lambda`,`rho`	Pointers to a vector with three entries. Required for Recursive Autonomous Predictor Based Subspace Identification (RAPBSID) and not discussed in this thesis.

A-5 Future work

There is much code written, but there are still some parts which can be improved. Some future work is listed:

- At this moment it is only possible to use first order polynomials with zero order continuity (i.e. $(d, r) = (1, 0)$). This could be extended to any (d, r) with $d \geq 1$, $r \geq 0$ and $d \geq r$.
- The reconstructed wavefront cannot be used as a mirror shape, because the wavefront is not at each point in the pupil plane defined. Therefore the triangulation has to be changed.

Bibliography

[1] D. Schweitzer, "How adaptive optics are improving cosmic observations," 2013. Accessed September 2014.

[2] K. Hinnen, *Data-Driven Optimal Control for Adaptive Optics*. PhD thesis, TU Delft, 1 2007.

[3] R. Marinica, C. Smith, and M. Verhaegen, "Adaptive optics based on intensity measurements," in *52nd IEEE Conference on Decision and Control*, 2013.

[4] D. P. Greenwood, "Bandwidth specification for adaptive optics systems," *J. Opt. Soc. Am.*, vol. 67, pp. 390–393, Mar 1977.

[5] R. Tyson, *Principles of Adaptive Optics*. CRC Press, 3 ed., 2010.

[6] C. Visser and M. Verhaegen, "Wavefront reconstruction in adaptive optics systems using nonlinear multivariate splines," *J. Opt. Soc. Am. A*, vol. 30, pp. 82–95, Jan 2013.

[7] J. Silva, E. Brunner, A. Polo, C. Visser, and M. Verhaegen, "Wavefront reconstruction using intensity measurement for real-time adaptive optics." -, 2013.

[8] S. Boyd, N. Parikh, E. Chu, B. Peleato, and J. Eckstein, "Distributed optimization and statistical learning via the alternating direction method of multipliers," *Found. Trends Mach. Learn.*, vol. 3, pp. 1–122, Jan. 2011.

[9] J. Herrmann, "Phase variance and strehl ratio in adaptive optics," *J. Opt. Soc. Am. A*, vol. 9, pp. 2257–2258, Dec 1992.

[10] T. S. Ross, "Limitations and applicability of the maréchal approximation," *Appl. Opt.*, vol. 48, pp. 1812–1818, Apr 2009.

[11] A. Chiuso, R. Muradore, and E. Fedrigo, "Adaptive optics systems: A challenge for closed loop subspace identifcation," in *American Control Conference, 2007. ACC '07*, pp. 2949–2954, 2007.

[12] D. G. MacMynowski, "Interaction matrix uncertainty in active (and adaptive) optics," *Appl. Opt.*, vol. 48, pp. 2105–2114, Apr 2009.

[13] R. E. Kalman, "A new approach to linear filtering and prediction problems," *Transactions of the ASME-Journal of Basic Engineering*, vol. 82, pp. 35–45, 1960.

[14] B. Platt and R. Shack, "History and principles of shack-hartmann wavefront sensing," *J. Refract. Surg.*, vol. 17, pp. 573–557, 2001.

[15] L. A. Poyneer, D. T. Gavel, and J. M. Brase, "Fast wave-front reconstruction in large adaptive optics systems with use of the fourier transform," *J. Opt. Soc. Am. A*, vol. 19, pp. 2100–2111, Oct 2002.

[16] C. de Visser and M. Verhaegen, "A distributed simplex b-spline based wavefront reconstructor," 2012. Accessed June 2014.

[17] A. N. Kolmogorov, "Dissipation of energy in locally isotropic turbulence," in *Doklady AN SSSR*, 1941.

[18] D. Bauer, "Order estimation for subspace methods," *Automatica*, vol. 37, no. 10, pp. 1561 – 1573, 2001.

[19] I. Rhodes, "A tutorial introduction to estimation and filtering," *Automatic Control, IEEE Transactions on*, vol. 16, no. 6, pp. 688–706, 1971.

[20] D. Simon, *Optimal state estimation.* John Wiley & Sons, 2006.

[21] C. Visser, *Global Nonlinear Model Identification with Multivariate Splines.* Dissertation, TU Delft, 7 2011.

[22] D. Gerwe, M. Johnson, and B. Calef, "Local minima analysis of phase diverse phase retrieval using maximum likelihood," in *Advanced Maui Optical and Space Surveillance Technologies Conference*, 2008.

[23] L. M. Mugnier, A. Blanc, and J. Idier, "Phase diversity: A technique for wave-front sensing and for diffraction-limited imaging," in *Advances in Imaging and Electron Physics* (P. Hawkes, ed.), vol. 141 of *Advances in Imaging and Electron Physics*, pp. 1 – 76, Elsevier, 2006.

[24] A. Quirrenbach, "The effect of atmosphere turbulence on astronomical observations," 2002.

[25] E. Hecht, *Optics.* Pearson Education Limited, 2001.

[26] W. Guo, L. Zhao, C. S. Tong, C. I-Ming, and S. C. Joshi, "Adaptive centroid-finding algorithm for freeform surface measurements," *Appl. Opt.*, vol. 52, pp. D75–D83, Apr 2013.

[27] L. A. Carvalho, "A simple and effective algorithm for detection of arbitrary hartmannâĂŞshack patterns," *Journal of Biomedical Informatics*, vol. 37, no. 1, pp. 1 – 9, 2004.

[28] R. Ragazzoni, "Pupil plane wavefront sensing with an oscillating prism," *Journal of Modern Optics*, vol. 43, no. 2, pp. 289–293, 1996.

[29] F. Roddier, "Curvature sensing and compensation: a new concept in adaptive optics," *Appl. Opt.*, vol. 27, pp. 1223–1225, Apr 1988.

[30] J. Hardy, *Adaptive Optics for Astronomical Telescopes*. Oxford series in optical and imaging sciences, Oxford University Press, 1998.

[31] R. J. Noll, "Zernike polynomials and atmospheric turbulence," *J. Opt. Soc. Am.*, vol. 66, pp. 207–211, Mar 1976.

[32] D. L. Fried, "Least-square fitting a wave-front distortion estimate to an array of phase-difference measurements," *J. Opt. Soc. Am.*, vol. 67, pp. 370–375, Mar 1977.

[33] R. H. Hudgin, "Wave-front reconstruction for compensated imaging," *J. Opt. Soc. Am.*, vol. 67, pp. 375–378, Mar 1977.

[34] W. H. Southwell, "Wave-front estimation from wave-front slope measurements," *J. Opt. Soc. Am.*, vol. 70, pp. 998–1006, Aug 1980.

[35] M. Rosensteiner, "Cumulative reconstructor: fast wavefront reconstruction algorithm for extremely large telescopes," *J. Opt. Soc. Am. A*, vol. 28, pp. 2132–2138, Oct 2011.

[36] M. Tallon, E. Thiébaut, and C. Béchet, "A fractal iterative method for fast wavefront reconstruction for extremely large telescopes," in *Adaptive Optics: Analysis and Methods/Computational Optical Sensing and Imaging/Information Photonics/Signal Recovery and Synthesis Topical Meetings on CD-ROM*, p. PMA2, Optical Society of America, 2007.

[37] C. R. Vogel, "Sparse matrix methods for wavefront reconstruction, revisited," 2004.

[38] A. Polo, V. Kutchoukov, F. Bociort, S. Pereira, and H. Urbach, "Determination of wave-front structure for a hartmann wavefront sensor using a phase-retrieval method," *Optics Express*, vol. 20, no. 7, pp. 7822–7832, 2012.

[39] W. H. Southwell, "Wave-front analyzer using a maximum likelihood algorithm," *J. Opt. Soc. Am.*, vol. 67, pp. 396–399, Mar 1977.

[40] X.-L. Hu, D.-F. Han, and M.-J. Lai, "Bivariate splines of various degrees for numerical solution of partial differential equations.," *SIAM J. Scientific Computing*, vol. 29, no. 3, pp. 1338–1354, 2007.

[41] G. Awanou, M. Lai, and P. Wenston, "The multivariate spline method for scattered data fitting and numerical solutions of partial differential equations," in *Wavelets and Splines: Athens 2005*, pp. 24–75, Nashboro Press, 2005.

[42] C. de Visser, Q. Chu, and J. Mulder, "Differential constraints for bounded recursive identification with multivariate splines," *Automatica*, vol. 47, no. 9, pp. 2059 – 2066, 2011.

[43] http://yorick.sourceforge.net/index.php, "Yorick home page." Accessed September 2014.

[44] F. Rigaut and M. Van Dam, "Simulating astronomical adaptive optics systems using yao," in *Proceedings of the Third AO4ELT Conference.* (S. Esposito and L. Fini, eds.), Dec. 2013.

[45] R. N. Tubbs, *Luck Exposures: Diffraction Limited Astronomical Imaging Through the Atmosphere*. PhD thesis, St John College Cambride University, 2003.

[46] K.-W. Roh, T.-K. Uhm, J.-Y. Kum, S.-K. Youn, and J. H. Lee, "Noise-insensitive centroiding algorithm for a shack-hartmann sensor," *Journal of the Korean Physical Society*, vol. 52, pp. 160–169, 2013.

[47] M. Verhaegen and V. Verdult, *Filtering and System Identification, A Least Squares Approach*. Cambridge University Press, 2007.

[48] P. van Overschee and L. de Moor, *Subspace identification for linear systems: theory, implementation, applications*. No. v. 1, Kluwer Academic Publishers, 1996.

[49] M. Verhaegen, "Identification of the deterministic part of mimo state space models given in innovations form from input-output data," *Automatica*, vol. 30, no. 1, pp. 61 – 74, 1994. Special issue on statistical signal processing and control.

[50] A. Chiuso, "The role of vector autoregressive modeling in predictor-based subspace identification," *Automatica*, vol. 43, no. 6, pp. 1034 – 1048, 2007.

[51] I. Houtzager, J. v. Wingerden, and M. Verhaegen, "Recursive predictor-based subspace identification with application to the real-time closed-loop tracking of flutter," *Control Systems Technology, IEEE Transactions on*, vol. 20, no. 4, pp. 934–949, 2012.

[52] J. van Wingerden, A. Hulskamp, T. Barlas, I. Houtzager, H. Bersee, G. van Kuik, and M. Verhaegen, "Two-degree-of-freedom active vibration control of a prototyped smart rotor," *Control Systems Technology, IEEE Transactions on*, vol. 19, no. 2, pp. 284–296, 2011.

[53] A. Chiuso, "On the asymptotic properties of closed-loop cca-type subspace algorithms: Equivalence results and role of the future horizon," *Automatic Control, IEEE Transactions on*, vol. 55, pp. 634–649, March 2010.

[54] D. Simon and T. L. Chia, "Kalman filtering with state equality constraints," *Aerospace and Electronic Systems, IEEE Transactions on*, vol. 38, no. 1, pp. 128–136, 2002.

[55] D. Simon, "Kalman filtering with state constraints: a survey of linear and nonlinear algorithms," *Control Theory Applications, IET*, vol. 4, no. 8, pp. 1303–1318, 2010.

[56] J. L. e Silva, "Distributed wavefront reconstruction for adaptive optics systems," Master's thesis, TU Delft, 2014.

[57] M. Lovera, T. Gustafsson, and M. Verhaegen, "Recursive subspace identification of linear and non-linear wiener state-space models," *Automatica*, vol. 36, no. 11, pp. 1639 – 1650, 2000.

Glossary

List of Acronyms

ADMM	Alternating Direction Method of Multipliers
AO	Adaptive Optics
APBSID	Autonomous PBSID
ASID	Autonomous Subspace Identification
CKF	Constrained Kalman Filter
DM	Deformable Mirror
KF	Kalman Filter
LLS	Linear Least Squares
LTI	Linear Time Invariant
MIMO	Multiple Input Multiple Output
PBSID	Predictor Based Subspace Identification
PME	Piston Mode Equalization
PO-ASID	Past Output ASID
PO-MOESP	Past Output Multivariable Output-Error State sPace
PSF	Point Spread Function
RASID	Recursive Autonomous Subspace Identification
SABRE	Spline based ABerration REconstruction
SH	Shack-Hartmann
SID	Subspace Identification

SVD	Singular Value Decomposition
WFR	Wavefront Reconstruction
WFS	Wavefront Sensor

List of Symbols

$\epsilon(\cdot)$	Residual wavefront, defined in equation (2-4)
κ	Multi-index with properties (3-11)
λ	Wavelength of light
$\phi(\cdot)$	Estimated phase with WFR
$\varphi(\cdot)$	Aberrations of the phase, e.g. due to atmospheric turbulence
$\psi(\cdot)$	The wavefront
$\sigma_x(\cdot), \sigma_y(\cdot)$	Slope measurements
$\tilde{\mathcal{K}}_s$	Extended controllability matrix, see (4-12)
$\mathcal{O}_s$	Extended observability matrix
A	State matrix
$b(x)$	Barycentric coordinates
$\mathbf{B}^d$	Evaluation vector which maps SABRE coefficients to the estimated phase point
C	Output matrix
c	Vector that contains all the (estimated) SABRE coefficients
D	Diameter of the telescope
d	Polynomial degree used for SABRE
e	Innovation vector
H	Constraint matrix that contains constraints for the SABRE coefficients c, see (3-26)
$\bar{H}$	A basis of the nullspace of H, i.e. $\text{null}\,(H)$
I	Intensity, i.e. square of the amplitude of a signal
J	Amount of (non-overlapping) simplices in which the wavefront domain is partitioned
K	Kalman matrix
K	Number of slope measurements
L	Number of different sub-domains
$P, P(\cdot)$	Performance indicator for the WFR
R	Performance indicator, which is used to indicate the performance of the predictions of the (C)KF
r	Continuity order used for SABRE
r	Spatial coordinate
r_0	Fried parameter
S	Strehl ratio, defined in equation (2-5)

$s(\cdot)$	Measurements from the Wavefront Sensor
k	Time instant
$u(\cdot), u(k)$	Output of the controller, input for actuator(s), e.g. at time instant k
$\hat{x}(\cdot)$	Predicted state vector
$\tilde{x}(\cdot)$	Predicted state vector such that the constraint (5-14) is met
x	State vector
x, y	Spatial coordinates
y	Output vector
Z	Complex amplitude of a wave

Index

ADMM, 2, 12, 47–49, 62
Anchor constraint, 18

Constrained prediction, 46
Coupling vectors, 50

Defocus aberration, 21, 26
Deformable Mirror, 6
Dual ascent method, 48

Focal plane sensors, 16
Fraunhofer diffraction, 14
Future window, 38, 39, 58, 68

Gauss-Seidel pass, 49
Gradient based SABRE, 10

Innovation, 34, 45
Innovation form, 34
Instrumental variable, 35
Intensity based SABRE, 2, 10

Kalman gain, 34
Kolmogorov model, 22

Lagrangian, 48–50
Local constraint matrix, 45
Local reduced data vector, 45

Maréchal's approximation, 8
Markov parameters, 37, 38
Method of Multipliers, 48
Modal measurements, 16
Model reduction method, 45

Non-uniqueness problem, 21

Past window, 37, 39, 58, 68
Performance indicator, 23
Piston Mode Equalization, 47, 58
Point Spread Function, 7
Predictor form, 34
Pupil plane sensors, 15

QR factorization, 36

Rayleigh criterion, 5
Reconstruction matrix, 67
Residual phase error, 7

Soft constraints, 63
State projection, 46–48, 58
State space model, 33
Strehl ratio, 7
Sub-domains, 45
Subspace Identification, 10

Temporal dynamics, 2, 43, 61
Triangulation, 23, 24, 52

Wavefront Sensor, 7

Yao, 2, 21, 51, 61, 62
Yorick, 22, 51, 62, 65

Zonal meaurements, 16